SANDIA REPORT
SAND2002-1406
Unlimited Release
Printed May 2002

Development of Magnetically Excited Flexural Plate Wave Devices for Implemenation as Physical, Chemical, and Acoustic Sensors, and as Integrated Micro-pumps for Sensored Systems

W. K. Schubert, D. R. Adkins, M. A. Mitchell, L. F. Anderson, D. C. Graf, R. J. Shul and K. O. Wessendorf

Prepared by
Sandia National Laboratories
Albuquerque, New Mexico 87185 and Livermore, California 94550

Sandia is a multiprogram laboratory operated by Sandia Corporation, a Lockheed Martin Company, for the United States Department of Energy under Contract DE-AC04-94AL85000.

Approved for public release; further dissemination unlimited.

Issued by Sandia National Laboratories, operated for the United States Department of Energy by Sandia Corporation.

NOTICE: This report was prepared as an account of work sponsored by an agency of the United States Government. Neither the United States Government, nor any agency thereof, nor any of their employees, nor any of their contractors, subcontractors, or their employees, make any warranty, express or implied, or assume any legal liability or responsibility for the accuracy, completeness, or usefulness of any information, apparatus, product, or process disclosed, or represent that its use would not infringe privately owned rights. Reference herein to any specific commercial product, process, or service by trade name, trademark, manufacturer, or otherwise, does not necessarily constitute or imply its endorsement, recommendation, or favoring by the United States Government, any agency thereof, or any of their contractors or subcontractors. The views and opinions expressed herein do not necessarily state or reflect those of the United States Government, any agency thereof, or any of their contractors.

Printed in the United States of America. This report has been reproduced directly from the best available copy.

Available to DOE and DOE contractors from
U.S. Department of Energy
Office of Scientific and Technical Information
P.O. Box 62
Oak Ridge, TN 37831

Telephone: (865)576-8401
Facsimile: (865)576-5728
E-Mail: reports@adonis.osti.gov
Online ordering: http://www.doe.gov/bridge

Available to the public from
U.S. Department of Commerce
National Technical Information Service
5285 Port Royal Rd
Springfield, VA 22161

Telephone: (800)553-6847
Facsimile: (703)605-6900
E-Mail: orders@ntis.fedworld.gov
Online order: http://www.ntis.gov/ordering.htm

SAND2002-1406
Unlimited Release
Printed May 2002

Development of Magnetically Excited Flexural Plate Wave Devices for Implementation as Physical, Chemical, and Acoustic Sensors, and as Integrated Micro-pumps for Sensored Systems

W. Kent Schubert, Mary-Anne Mitchell, Darin C. Graf, and Randy J. Shul
Microdevice Technologies Department

Douglas R. Adkins and Larry F. Anderson
Micro Analytical Systems Department

Kurt O. Wessendorf
Frequency Devices Department

Sandia National Laboratories
P.O. Box 5800
Albuquerque, NM 87185-0603

Abstract

The magnetically excited flexural plate wave (mag-FPW) device has great promise as a versatile sensor platform. FPW's can have better sensitivity at lower operating frequencies than surface acoustic wave (SAW) devices. Lower operating frequency (< 1 MHz for the FPW versus several hundred MHz to a few GHz for the SAW device) simplifies the control electronics and makes integration of sensor with electronics easier. Magnetic rather than piezoelectric excitation of the FPW greatly simplifies the device structure and processing by eliminating the need for piezoelectric thin films, also simplifying integration issues. The versatile mag-FPW resonator structure can potentially be configured to fulfill a number of critical functions in an autonomous sensored system. As a physical sensor, the device can be extremely sensitive to temperature, fluid flow, strain, acceleration and vibration. By coating the membrane with self-assembled monolayers (SAMs), or polymer films with selective absorption properties (originally developed for SAW sensors), the mass sensitivity of the FPW allows it to be used as biological or chemical sensors. Yet another critical need in autonomous sensor systems is the ability to pump fluid. FPW structures can be configured as micro-pumps. This report describes work done to develop mag-FPW devices as physical, chemical, and acoustic sensors, and as micro-pumps for both liquid and gas-phase analytes to enable new integrated sensing platform.

Acknowledgements

The authors would like to acknowledge major contributions to and continual support of this work by Stephen J. Martin and Michael A. Butler. Many of the original ideas for the magnetically excited flexural plate wave device came from them. They were both major contributors earlier in the project before other assignments pulled them to other duties. Robert Waldschmidt also contributed much during his time at Sandia National Laboratories, but has also gone on to a new job. We sincerely thank all three of these men for their contributions and support, and wish them the best in their current endeavors.

CONTENTS

Abstract 3
Acknowledgements 4
Introduction 6
Basic Operating Principles 7
Higher-Order Resonators 7
Fundamental Mode Single-Port Resonators 12
Design & Process Description 14
Membrane requirements 14
Fabrication Methods for Si-Based FPWs 15
Wet Etch Protocol 15
DRIE Protocol 17
Characterization Methods 26
Dimensional Characterization 26
Network Analysis 26
Mode Imaging 27
Modeling 28
General Characterization Results for FPW resonators 30
Higher Order Resonators 30
KOH-Etched Devices 30
DRIE Processed FPW Resonators 40
Fundamental Mode Resonators 44
Chemical sensors 46
Accelerometers 50
Gas Phase Flow Sensors 56
Liquid Operation 60
Summary and Future Directions 61
Summary and Future Directions 62
Appendix A. Bulge Measurements of Membrane Stress 65
Appendix B. Portable Drive Electronics 69
Two-Port mag-FPW Resonator Oscillator Circuitry 69
1-Port Hand-Held Instrumentation 73
Appendix C – KOH Fabrication Process for mag-FPWs 75
Appendix D – DRIE Process for mag-FPW Accelerometers 77
References 80

Introduction

White and Wenzel have shown that flexural plate waves (FPWs) can be excited in a free-standing membrane formed on a silicon substrate[1,2]. Included in the layers of their composite membrane are a piezoelectric ZnO layer and interdigital transducers that are used to excite the FPWs. In an alternative approach, Giesler and Meyer have shown that electrostatic excitation can also be used to excite these waves[3]. Exciting waves in a thin membrane, as opposed to a thick substrate as in a SAW device, results in a lower operating frequency and, consequently, simpler oscillator electronics. In addition, the confinement of acoustic energy in a thin membrane makes the wave velocity more sensitive to surface perturbations, e.g., accumulation of mass. This results in greater sensitivity in sensing applications[2].

In this report we describe a new FPW device that uses a meander-line electrode pattern on the membrane surface, in combination with a static in-plane magnetic field, to excite and detect flexural plate waves[4,5]. A generic schematic of a magnetically-excited FPW (mag-FPW) resonator is shown in Fig. 1. The flexural plate waves are excited in a bounded membrane that acts as a resonant cavity, giving rise to a hiqh quality factor (Q), and thus a narrowband response. This results in a greater vibrational amplitude for a given input power and greater frequency stability when used in an oscillator circuit.

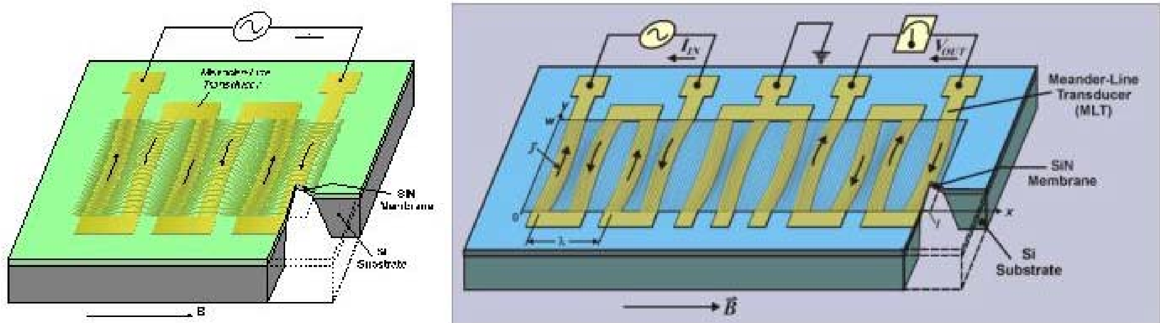

Fig. 1. Schematic drawings of single-port (left) and two-port mag-FPW resonators. Excitation of a rectangular membrane mode is achieved by Lorentz forces generated between an alternating current in a meander- line transducer and a static in-plane magnetic field.

Part of the purpose of this LDRD project was to develop the silicon-based mag-FPW structure for sensor system applications. The versatile FPW platform can in principle, serve several functions in such a system as indicated in Figure 2. Elimination of the thin film piezoelectric layer in traditional FPW technology simplifies the fabrication process and should make it easier to integrate the sensors and actuators on-chip with Si-based control electronics. This concept guided many of the areas investigated in this project. As things progressed, we also began to investigate a second embodiment of the FPW structure, this time in flexible circuit board technology. The flex circuit version is even simpler to make, but requires hybrid integration with the control electronics.

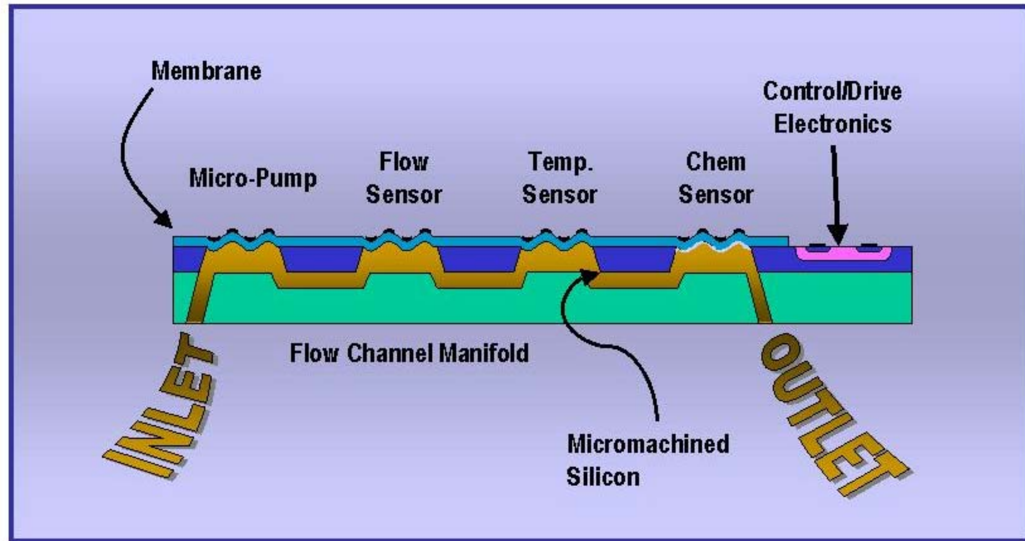

Fig. 2. Schematic drawing of a sensored system where the mag-FPW device structure performs a number of different sensing and actuation functions.

In the following sections we will discuss the basic operating principles of the mag-FPW resonator. We will describe the key characteristics and how they relate to fabrication methods and ultimate performance. Finite element modeling results will be compared with the experimental data. Finally, we will discuss applications of mag-FPW devices as chemical sensors, accelerometers, flow sensors, and micropumps.

Basic Operating Principles

Higher-Order Resonators

The operation of the meander-line transducer (MLT) and magnetic field in exciting and detecting FPWs is illustrated in Fig. 1. Current lines, running across the width of the membrane, are positioned at regular intervals on the insulating membrane surface. When a static, in-plane magnetic field is applied perpendicular to the current direction, a surface-normal Lorentz stress (force per area) $\vec{F}$ is generated:

$$\vec{F} = \vec{J} \times \vec{B} \qquad (1)$$

where $\vec{J}$ is the two-dimensional current density on the membrane surface and $\vec{B}$ is the magnetic flux density. The reversing current direction between successive current lines generates spatially-alternating surface-normal Lorentz forces ($F_z = B_x J_y$). Proper positioning of these current lines with respect to the membrane boundaries allows excitation of an eigenmode of the rectangular membrane.

The MLT serves to detect membrane resonances as well as excite them. In a one-port device (left panel of Fig. 1), motion of the MLT in the magnetic field generates an impedance change that can be used to track membrane resonance: an electromotive force (emf) is induced due to motion of the conductor in the magnetic field. This shows up as an impedance peak at resonance. In a two-port device (right panel of Fig. 1), the membrane resonance excited by forcing an ac current in a first (input) transducer produces motion that generates a voltage on a second (output) transducer. The two transducers are separated by grounded dummy transducer lines to minimize direct coupling between the input and output ports.

A rather complete description of the equivalent circuit model of the mag-FPW resonator is given in Martin, etal[6]. We will cover only key elements of that description here. Referring to the geometry of Fig. 1, the surface-normal membrane displacement u generated by the distributed Lorentz force is determined by[7]:

$$D \, \Delta^4 u \; - \; T \, \Delta^2 u \; + \; Z_a \, \dot{u} \; + \; \rho_s \, \ddot{u} \; = \; - \, B_x \, J_y \qquad (2)$$

where D, T, and ρ_s are the membrane bending moment, tension (force per edge length), and areal mass density, respectively; Z_a is a mechanical impedance arising from fluid loading (gas or liquid). The tension T is equal to the product of the residual (in plane) stress in the membrane (σ) and the membrane thickness. The bending moment $D = Eh_1^3/[12(1 - v^2)]$, where E is Young's modulus, v is Poisson's ratio, and h_1 is the membrane thickness. Internal membrane damping can be included by using a complex Young's modulus $E^* = E(1 + j\delta)$, where δ is the loss tangent, in calculating the bending moment[8]. This equation can be solved in two limits. We examine only linear solutions here that apply for small-amplitude oscillations, since this is the normal operating mode for sensor applications. The reader is referred to reference 6 for a discussion of nonlinear solutions.

A rectangular membrane supported at the edges can be excited into a number of eigenmodes. Provided the membrane is thin compared to an acoustic wavelength, these eigenmodes can be found analytically in the linear regime, with displacement given as a superposition of normal modes[9]:

$$u(x, y, t) \; = \; \sum_{m=1}^{\infty} \sum_{n=1}^{\infty} A_{mn} \, \sin(k_m x) \, \sin(k_n y) \, e^{j\omega t} \qquad (3)$$

where A_{mn} is the complex displacement amplitude of the (m,n) eigenmode; $k_m = m\pi/l$ and $k_n = n\pi/w$, where l and w are the membrane length and width, respectively, and m and n are integers denoting the longitudinal (in the x-direction) and transverse (y-direction) mode variations; $\omega = 2\pi f$, where f is the excitation frequency. The left panel of Figure 1 shows the membrane of a single port device being excited into an m=6, n=1 mode (or 6-1 mode), while the right panel shows the 11-1 mode excited in a two-port device.

Allowing for the possibility of either one or two MLTs on the membrane (one- or two-port devices), the eigenmode amplitude A_{mn} generated is:

$$A_{mn} \; = \; - \, \frac{2}{j\,\omega\,(w\,l\,)^{1/2}} \left(\frac{K_{mn}^{(1)} \, \hat{I}_1 + K_{mn}^{(2)} \, \hat{I}_2}{Z_{mn}} \right) \qquad (4)$$

where $\hat{I}_1$ and $\hat{I}_2$ are the current amplitudes in transducers 1 and 2, while $K_{mn}^{(1)}$ and $K_{mn}^{(2)}$ are the respective transducer *coupling strengths* to the (m,n) membrane mode (for a one-port device, $K_{mn}^{(2)}\hat{I}_2=0$); Z_{mn} is the *mechanical impedance* (ratio of surface-normal stress to particle velocity) associated with exciting the mode:

$$Z_{mn} = \frac{D\,k_{mn}^4}{j\,\omega} + \frac{T\,k_{mn}^2}{j\,\omega} + j\,\omega\,\rho_s + \frac{D\,\delta\,k_{mn}^4}{\omega} + Z_a \tag{5}$$

where $k_{mn} = (k_m^2 + k_n^2)^{½}$.

Membrane resonances occur at excitation frequencies for which the imaginary part of Z_{mn} vanishes. In a vacuum, where $Z_a = 0$, this occurs at angular frequencies:

$$\omega_{mn} = k_{mn}\left(\frac{D\,k_{mn}^2 + T}{\rho_s}\right)^{\frac{1}{2}}. \tag{6}$$

In a fluid, where Z_a is a complex quantity, the frequency will be shifted due to the fluid loading on the membrane. At resonance, membrane displacement is maximum, limited only by the loss parameters Z_a and δ.

As mentioned above, the MLT impresses a surface current density $J_y(x,y)$ in a manner designed to preferentially excite a particular membrane mode. The mode coupling factor $K_{mn}^{(i)}$ is proportional to the *spatial correlation* between the current density $J_y(x,y)$ and the (m,n) eigenmode displacement profile:

$$K_{mn}^{(i)} = \frac{2\,B_x}{(w\,l\,)^{1/2}\;\hat{I}_i}\int_0^w\int_0^l \hat{J}_y^{(i)}(x,y)\,\sin(k_m\,x)\,\sin(k_n\,y)\,dx\,dy \tag{7}$$

where $\hat{J}_y^{(i)}$ is the amplitude of the current density applied by the ith MLT (i = 1,2). Assuming the current lines are infinitesimally wide, with current alternating in direction between lines, the coupling factor is:

$$K_{mn}^{(i)} \cong \frac{2 B_x}{\pi} \left(\frac{w}{l}\right)^{\frac{1}{2}} \left[\frac{1 - (-1)^n}{n}\right] \sum_{p=1}^{2N} (-1)^{p+1} \sin(k_m x_p) \tag{8}$$

where N is the number of MLT periods. (N may be as large as $m/2$ if every longitudinal antinode has a current line.) Equation 8 applies for arbitrary positioning of the current lines.

Efficient coupling to a particular longitudinal (index m) mode can be achieved by positioning current lines along the longitudinal mode maxima, i.e., centered at $[\lambda/4 + p(\lambda/2)]$, where λ is the longitudinal mode wavelength and p is an integer. The MLT couples preferentially to the longitudinal mode that has periodicity equal to that of the MLT. This means that $\sin(k_m x_p) = (-1)^p$ so that the sum in Eq. 8 is equal to $2N$. When the current lines extend across the width of the membrane, as pictured in Fig. 1, the Lorentz force is uniform across the membrane width and does not match the fundamental transverse mode profile. As indicated in Eq. (8), this uniform force distribution couples to a family of odd-order transverse modes (n = 1, 3, 5...), with coupling strength varying as n^{-1}.

The voltage $V_i = \hat{V}_i e^{j\omega t}$ across the ith MLT has contributions from ohmic resistance in the line and a back emf due to motion of the conductor in the magnetic field:

$$\hat{V}_i = \hat{I}_i R_{oi} - \frac{\partial}{\partial t} \int \vec{B} \bullet \hat{x} \, dA \tag{9}$$

where i indicates the transducer and R_{oi} is the associated ohmic resistance; the integration occurs over the area (with normal $\hat{x}$) defined by the displaced MLT lines:

$$\hat{V}_i = \hat{I}_i R_{oi} - j \omega B_x \sum_{p=1}^{\infty} (-1)^{p+1} \int_0^w \hat{u}(x_p, y) \, dy. \tag{10}$$

where $\hat{u}$ is the membrane displacement contour ($u = \hat{u} e^{j\omega t}$). Combining Eqs. 3, 4, 8, and 10 gives

$$\hat{V}_i = \hat{I}_i R_{oi} + \sum_{m=1}^{\infty} \sum_{n=1}^{\infty} K_{mn}^{(i)} \left(\frac{K_{mn}^{(1)} \hat{I}_1 + K_{mn}^{(2)} \hat{I}_2}{Z_{mn}} \right). \tag{11}$$

Using Eq. 11, the voltages (V_1, V_2) and currents (I_1, I_2) at the ports of a one- or two-port mag-FPW resonator can be related:

$$\begin{pmatrix} \hat{V}_1 \\ \\ \hat{V}_2 \end{pmatrix} = \begin{pmatrix} R_{o1} + \sum_{m=1}^{\infty} \sum_{n=1}^{\infty} \frac{\left(K_{mn}^{(1)}\right)^2}{Z_{mn}}, & \sum_{m=1}^{\infty} \sum_{n=1}^{\infty} \frac{K_{mn}^{(1)} K_{mn}^{(2)}}{Z_{mn}} \\ \\ \sum_{m=1}^{\infty} \sum_{n=1}^{\infty} \frac{K_{mn}^{(1)} K_{mn}^{(2)}}{Z_{mn}}, & R_{o2} + \sum_{m=1}^{\infty} \sum_{n=1}^{\infty} \frac{\left(K_{mn}^{(2)}\right)^2}{Z_{mn}} \end{pmatrix} \begin{pmatrix} \hat{I}_1 \\ \\ \hat{I}_2 \end{pmatrix}. \tag{12}$$

The 2×2 matrix on the right-hand side of Eq. (12) is the impedance or *Z-matrix* for the resonator. Taking $\hat{I}_2$ as zero, this model applies to the one-port device also.

For a one-port device, we typically use the *input impedance* Z_{11} to track membrane resonances. Using Eq. (12) with $\hat{I}_2 = 0$ gives:

$$Z_{11}(\omega) = \left.\frac{\hat{V}_1}{\hat{I}_1}\right|_{\hat{I}_2=0} = R_{o1} + \sum_{m=1}^{\infty} \sum_{n=1}^{\infty} \frac{\left(K_{mn}^{(1)}\right)^2}{Z_{mn}}. \tag{13}$$

In a two-port resonator, the *transmission response* (scattering parameter), S_{21}, the ratio of the output voltage to the input voltage, is typically used to track resonances and is given by[10]:

$$S_{21} = \frac{2\, z_{21}}{(z_{11} + 1)(z_{22} + 1) - z_{12}\, z_{21}} \tag{14}$$

where z_{11} etc. are elements of the Z-matrix in Eq. (12), normalized to the test system characteristic impedance Z_0 (typically 50 Ω): $z_{ij} = Z_{ij}/Z_0$.

The above discussion gave the response arising from *all* eigenmodes (m,n) that can be excited in a rectangular membrane. We noted that a single longitudinal m-mode can be preferentially excited by proper positioning of current lines on the antinodes for this mode. The associated n = 1 transverse mode is most efficiently excited and can be targeted for use. When exciting the device over a narrow frequency range near this isolated mode, the previous model can be simplified by using only the single term in the summations that corresponds to this mode.

For a transducer positioned optimally to couple to a particular m mode, and considering coupling to only the fundamental (n=1) transverse mode, Eq. 8 gives the coupling factor as:

$$K_i = \frac{8\, B_x\, N\, e}{\pi} \left(\frac{w}{l}\right)^{\frac{1}{2}} \tag{15}$$

(the mn subscripts on $K_{mn}^{(i)}$ have been dropped) where e is a *coupling efficiency* equal to unity in the ideal case but less in practice due to the finite width of the conductor and imperfect MLT positioning.

From Eq. (12) the voltages (V_1, V_2) and currents (I_1,I_2) near an isolated mode are related by

$$\begin{pmatrix} \hat{V}_1 \\ \hat{V}_2 \end{pmatrix} = \begin{pmatrix} R_o 1 + \frac{K_1^2}{Z_{mn}}, & \frac{K_1 K_2}{Z_{mn}} \\ & \end{pmatrix} \begin{pmatrix} \hat{I}_1 \\ \end{pmatrix}. \quad (16)$$

$$Z_{11}(\quad (17)$$

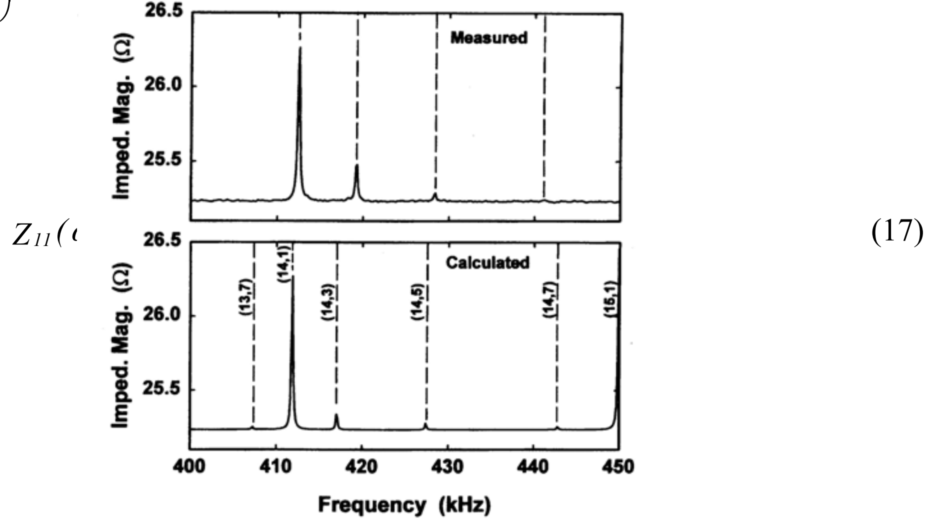

Figure 3. Broadband scan of the impedance response (Z_{11} vs f) for a one-port mag-FPW resonator showing the transverse mode spectrum. The response was calculated using Eqs. (5), (13), and (15).[6]

The input impedance for the one-port device is then:
and the transmission response is found from Eq. (14) using the Z elements from Eq. (16).

Figure 3 shows a broadband scan of the input impedance $Z_{11}(f)$ of a one-port device, revealing the *mode spectrum* (calculated and measured). This device has 7 MLT periods with a periodicity λ = 320 µm. The SiN membrane dimensions are nominally l=7λ=2.2 mm, w = 10λ = 3.2 mm, and h_1 = 2 µm. In calculating the broadband response, we use the linear model that accounts for all rectangular membrane modes [Eqs. (13) and (8)]. In the calculation we use the D, T_o, and ρ_s values determined for the particular device[6], along with the membrane dimensions. The calculated response, in qualitative agreement with the measured response, shows that the fundamental transverse mode (m,1) is most strongly excited; odd-order transverse modes (m,n) are excited at successively higher frequencies, but with diminishing amplitudes.

Fundamental Mode Single-Port Resonators

In contrast to the higher-order mag-FPW resonators that set up a standing wave with several wavelengths across a rectangular membrane (Fig. 1), the fundamental-mode device shown in Fig. 4 uses a circular membrane and attempts to set up a mode where the entire membrane moves up and down together. The single-port transducer is laid out so that the Lorentz force on all of the lines is always in the same direction. The operation of these devices has been described in considerable detail in the Masters thesis of M. K. Hill[11]. As with the higher-order devices discussed above, only key elements of the description will be covered here.

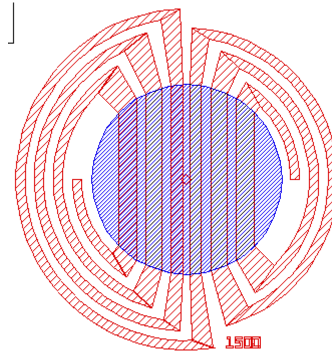

Figure 4. Layout of the transducer pattern (red) with respect to the circular membrane (blue) of a fundamental mode mag-FPW resonator. The single port transducer is configured to cause the entire membrane to oscillate up and down together (i.e. in the fundamental mode).

The resonant frequency of the fundamental-mode FPW resonator is given by an equation of the form:

$$\omega = \frac{1}{l}\sqrt{\frac{C_1 \sigma}{\rho}} \tag{18}$$

where ω is the circular resonant frequency, σ is the residual stress (in plane) in the membrane, ρ the effective density, l is the membrane diameter, and C_1 is a constant whose value depends upon the shape of the membrane[11]. C_1 would be 4 for an ideal, circular membrane. This general dependence holds as long as the diameter is large enough, and the membrane thickness small enough that the bending moment of the membrane does not begin to have a significant effect.

Design & Process Description

Membrane requirements

As is clear from the resonant frequency equation given above (Eq. 6), the membrane is one of the key elements in the FPW device. Its dimensions and material properties (areal mass density, bending moment, and tension) determine the acoustic characteristics of the device. In the course of this project we evaluated several materials as membrane candidates, including silicon-rich, low-stress silicon nitride (SiN) deposited by low pressure chemical vapor deposition (LPCVD), amorphous diamond-like carbon films (a-D) deposited by a laser ablation process, a variety of plasma-enhanced chemical vapor deposited (PECVD) films (including SiN, SiC, and SiO_xN_y), and finally a spin-on polymer film (BCB).

Over the course of the project LPCVD SiN films were obtained from three external sources. Very early in the project we used SiN films obtained from Professor Tom Kenny at Stanford University. The films ranged up to 2-μm in thickness. Residual stress in the films ranged from about 60 – 150 MPa. Since these films were not very repeatable and available only in small numbers, most later work was done using 0.5-μm SiN films obtained from the Microelectronics Center of North Carolina (MCNC), which eventually evolved into a start up company called Chronos. These films typically had residual stress ranging from 100-150 MPa. Chronos was eventually bought out by JDS Uniphase and stopped functioning as an external supplier of silicon micromachining substrates. This forced us to find yet another source of LPCVD SiN films, Delft University in Belgium. These films ranged up to 1-μm thick, and had properties very similar to the MCNC films. Some of these wafers included an underlying SiO_2 layer to act as an etch stop for the DRIE process discussed below.

During the latter parts of the project we also occasionally used LPCVD SiN films obtained from Sandia's Microelectronics Development Laboratory (MDL). These films were obtainable only on 150-mm wafers. Since most of our processing equipment cannot handle 150-mm wafers, we had to process quarter-wafer pieces when using this material. In addition, all of our photomask sets were designed for 100-mm wafers.

A variety of plasma-enhanced chemical vapor deposited (PECVD) dielectric films were screened for applications in silicon-based (FPW) devices. All films were deposited with the Plasma-Therm 790 PECVD system in the Compound Semiconductor Research Lab (CSRL) and included silicon carbide, silicon oxynitride, silicon oxycarbide, and silicon carbynitride all deposited from a silicon source of trimethylsilane. These efforts involved variation of the deposition conditions and/or post deposition anneals conditions. The films were evaluated for intrinsic film stress and etch resistance in the deep reactive ion etch (DRIE) and potassium hydroxide (KOH) silicon etch. As-deposited stress measurements for these films ranged from 158 MPA compressive for silicon carbide to 1048 MPA tensile for silicon oxycarbide. Only silicon carbide showed acceptable etch resistance in the KOH etch and DRIE process. However, we were not able to simultaneously achieve low tensile stress and maintain this etch resistance. Due to the above results, we stopped work on PECVD films for FPW membrane applications.

Finally, BCB (bisbenzocyclobutene) polymer membranes were investigated for FPW devices fabricated using the DRIE protocol described below (BCB is not

compatible with the KOH etch solution). This material (Cyclotene from the Dow Chemical Company) is a spin on polymer film developed as an interlevel dielectric for microelectronic applications. Cyclotene refers to a family of high-purity polymer solutions derived from B-staged bisbenzocyclobutene (BCB) monomers, formulated as high-solids, low-viscosity solutions. Notable properties of the resins of interest for the present application include: low dielectric constant, low loss at high frequency, low moisture absorption, low cure temperature, high degree of planarization, low level of ionics, high optical clarity, good thermal stability, excellent chemical resistance,and good compatibility with various metallization systems. The resins are available in photosensitive and dry-etch grades.

Fabrication Methods for Si-Based FPWs

Appendices C and D include typical "runsheets" for fabrication of the various FPW devices. These runsheets can be consulted for the detailed processing protocol. A few of the essential features are discussed below. We have used two basic methods to fabricate mag-FPW devices. An anisotropic silicon etch is used in both methods, but in one case it is a wet etch (hot KOH solution), in the other, dry (the so-called "Bosch etch"[12], also called a deep reactive ion etch, DRIE). The wet etch method will be described first. The more versatile dry etch process is then described.

Wet Etch Protocol

Excellent descriptions of bulk silicon micromachining using anisotropic wet etches such as potassium hydroxide (KOH), tetramethyl ammonium hydroxide (TMAH), and ethylene diamine pyrocatechol (EDP) are available in the literature[13,14] and will not be reviewed here. For the present discussion it is sufficient to point out that when using these etch solutions on (100) Si wafers, the etch rate of the Si (111) planes is essentially nil. With careful alignment of rectangular or square patterns with the <110> directions of the wafer, one can produce very precise features, such as trapezoidal pits with V-shaped bottoms, or released membranes of a low-stress, etch resistant material such as SiN (see discussion above).

These methods were used to fabricate the majority of the SiN membrane FPW devices used in this study. The 400 μm thick starting wafers are polished on both sides, and coated with LPCVD low-stress silicon nitride. In order to precisely control membrane sizes and alignment of important structures, extra patterning and etching steps were used to precisely locate the <110> directions on the (100) Si wafer (2). Etch windows in the backside nitride were aligned to the <110> directions, and opened with a plasma etch. Front surface aluminum transducers were formed using a lift-off process and were precisely centered within the backside etch windows. The membranes were released using a KOH etch solution. The wafer thickness is critical in determining the size of the released membranes. Apiezon black wax was used to protect the aluminum metalization during the KOH etch. Finally the wax was dissolved in trichloroethylene, and the wafers rinsed in acetone and methanol. This fabrication protocol provided excellent control of critical dimensions.

The major steps in the wet-etch fabrication process for mag-FPW devices are depicted in Fig. 5. A (100) silicon wafer, polished on both sides, is coated on both sides with a low-stress silicon nitride (or other suitable etch resistant) layer. On the front side, this layer will act as the dielectric FPW membrane. On the backside, it will act as a mask for the anisotropic Si etch. A photoresist layer is then patterned on the backside to define the openings for the FPW membranes. These openings must be precisely aligned to the <110> planes of the Si wafer[13] because the subsequent anisotropic Si etch will naturally align the membrane edges to these directions (the etch rate on <111> planes is dramatically lower). Misalignment of these openings to the <110> planes causes the membranes to be larger than intended, making it less efficient to excite the intended resonant mode in the FPW membrane. The photoresist openings must also be larger than the intended membrane size to account for the 54.7^{o} angles of the <111> planes left behind by the wet etch. A dry etch is used to remove the SiN from the windows patterned in the photoresist layer. Next the metal MLTs are patterned on the front side of the wafer. Double-sided alignment is used to ensure proper positioning of the MLTs with

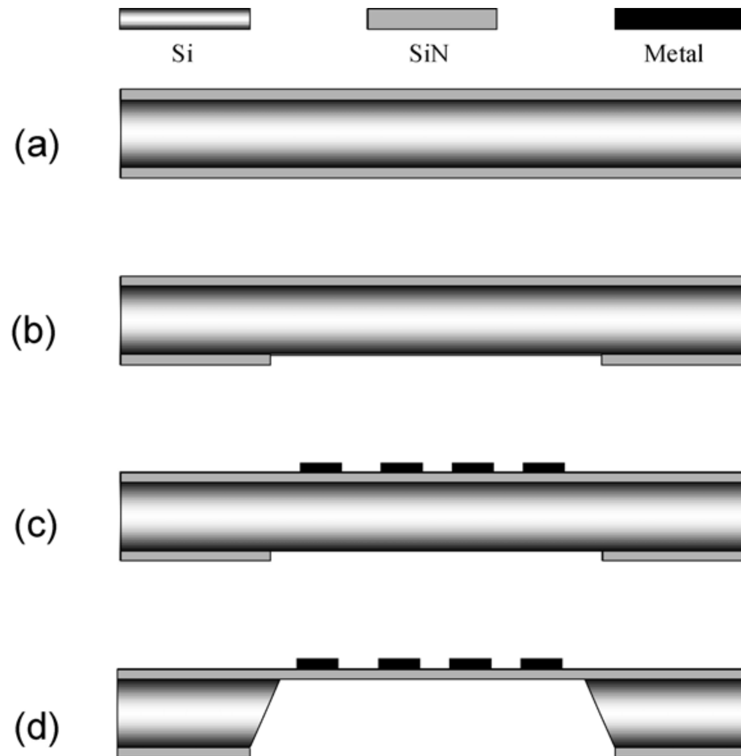

Fig 5. Cross sectional representations of the key steps in the fabrication of mag-FPW resonators using the KOH etching process to release the membranes. The LPCVD SiN membrane coats both sides of the wafer in (a). An etch window opened in the back side nitride is precisely aligned to the (110) directions of the wafer (b). In (c) the metal pattern on the front side is precisely centered within the backside etch window using double-sided alignment methods. Finally, the silicon is etched away in the KOH solution to release the membrane. The <111> planes define the sloped walls of the etched silicon.

respect to the eventual FPW membranes so that the proper mode will be excited. The final step is to release the FPW membranes using the anisotropic Si etch (85°C, 35% KOH solution). Since the aluminum is attacked by the KOH solution, the front side is protected by Apiezon black wax during the KOH etch. Trichloroethylene, followed by acetone and methanol are used to remove the black wax after the Si is completely removed from beneath the FPW membrane.

DRIE Protocol

The above KOH fabrication method is limited by the crystallography of the material. While the simple rectangular membrane FPW devices used for many of the applications are made by this method, some of the more complicated shapes, such as those required for the vibration and accelerometer sensors, require a more versatile fabrication method.

Recently, new bulk micromachining processes based on plasma etching at high rates have been developed. This approach addresses many of the limitations of wet chemical micromachining since the pattern fidelity is not limited by crystallography, selectivity, or directionality. To date, most work reported in the literature in this area has been done with research tools, or with very large features.[15,16] The utilization of high-density plasmas (HDP) including electron cyclotron resonance (ECR) and inductively coupled plasma (ICP) etch systems and the development of the "Bosch" deep reactive ion etch (DRIE) process[17] has contributed significantly to the development of high-aspect ratio, deep Si etching.[18,19,20,21,22,23] HDP etch systems typically yield higher etch rates under less energetic ion conditions than more conventional reactive ion etch (RIE) systems. This has been attributed to plasma densities that are 2 to 4 orders of magnitude higher and the ability to effectively decouple ion energy and plasma density. Etch profiles also tend to be more anisotropic due to lower process pressures which results in less collisional scattering and greater directionality of the plasma species.

In general, plasma etching involves two general mechanisms: a) physical sputtering and b) chemical reactions. Plasma etch processes can be further categorized into 4 basic groups: a) sputtering, b) chemical etching, c) ion-enhanced etching, and d) sidewall inhibitor etching. In sputtering, ions are accelerated as they cross the plasma sheath, which is formed just above the substrate. The ions transfer large amounts of energy (> 100 eV) and momentum to the surface, thereby removing material. The etch profile is often tapered and can result in significant damage, low etch selectivity, and rough surface morphology, thus impairing device performance.

In chemical etching the process consists of the following series of steps: a) production of reactants in the plasma; b) transport of reactants to the substrate surface; c) adsorption of reactants onto the substrate surface; d) chemical reaction; and e) desorption of volatile etch products from the surface. In order for this process to be successful, reactive neutrals must form volatile etch products during the reaction with the surface. Since there is little or no physical ion bombardment associated with this mechanism, the removal rate of material laterally tends to be similar to the removal rate of material in the vertical direction. This can result in significant undercutting of the mask and loss of critical dimension. However, with no ion bombardment, plasma-induced damage can be quite low and etch selectivity can be quite high depending on the volatility of etch products formed.

Anisotropic patterning can often be obtained by either ion-enhanced etching or sidewall inhibitor etching. In ion-enhanced etching both physical and chemical etching are employed. Due to the perpendicular nature of the ions accelerated across the plasma sheath to the surface of the sample, anisotropic profiles are obtained. The ions also provide energy/momentum transfer to improve sputter desorption of volatile etch products formed on the surface. For sidewall inhibitor etching, a polymer forming gas is added to the plasma chemistry to initiate the formation of a thin film on the sidewalls of the etched feature. Provided the ion scattering is low (low mean free path), the sidewall polymer film remains intact and acts as an etch barrier, preventing lateral etching and thus yielding anisotropic etch profiles.

As mentioned above, pattern transfer into Si has been very successful by both wet chemical and plasma etch techniques. However, the fabrication of deep, high-aspect ratio Si structures has been limited due to low etch selectivity to photoresist masks, slow etch rates, and/or poor lateral dimensional control. The recent development of a DRIE Si etch process has resulted in anisotropic profiles at room temperature, etch rates > 3.0 µm/min, aspect ratios > 30:1, and good dimensional control.[19-23] Additionally, the DRIE process has shown etch selectivities of Si to photoresist > 75:1 thereby eliminating the process complexity of hard etch masks for features deeper than 100 µm.

The DRIE process (patented by Robert Bosch GmbH[17]) has similarities to sidewall inhibitor etching mentioned above. DRIE relies on an iterative ICP-based deposition/etch cycle in which a polymer etch inhibitor is conformally deposited over the wafer during the deposition cycle. This is displayed schematically in Figure 6. The polymer deposits conformally over the resist mask, the exposed Si field, and along the sidewall of the mask. During the ensuing etch cycle, the polymer film is preferentially sputtered from the Si trenches and the top of the resist mask due to the acceleration of ions (formed in the ICP plasma) perpendicular to the surface of the wafer. Provided the ion scattering is relatively low, the polymer film on the sidewall is removed at a much slower rate, thus minimizing lateral etching of the Si. Before the sidewall polymer is completely removed, the deposition step is repeated and the cycle continues until the desired etch depth is obtained.

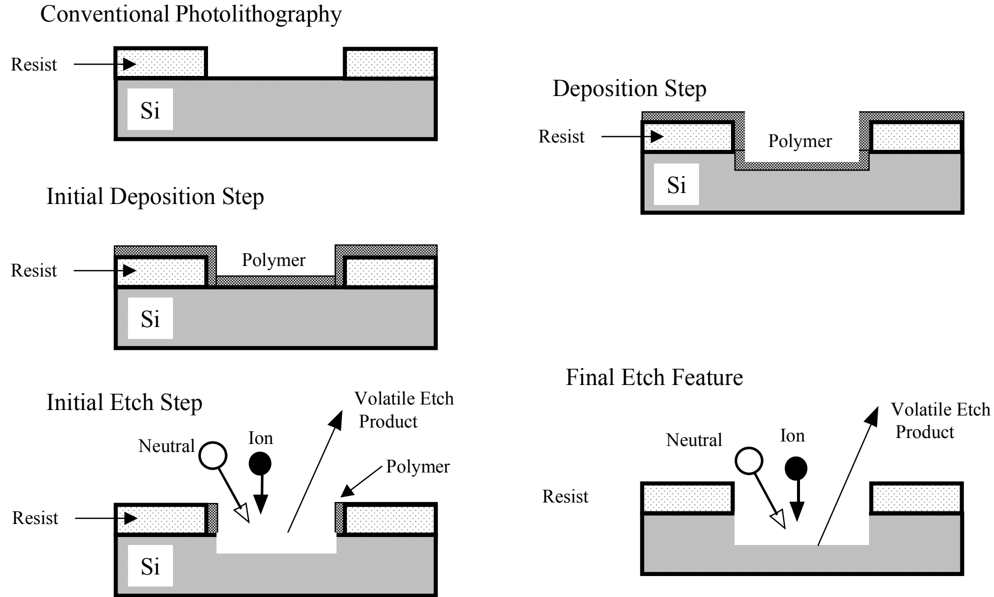

Figure 6. Schematic diagram of the deep reactive ion etch (DRIE) "Bosch" process.

The DRIE process has many advantages for the fabrication of the FPW device including the option for post-processing and simplification as compared to wet chemical etching. Key characteristics of the DRIE process includes the high etch selectivity for etching Si with respect to low-stress SiN (~80:1) (the material of the front side FPW membrane) or photoresist (~50:1); anisotropic straight-wall profiles; and dimensional control (non-crystallographic etching). This enables high control of critical dimensions for closer spacing of structures as well as increased freedom in the design of structures.

The single-step DRIE process for the FPW is summarized below and shown schematically in Figure 7. A 100 mm, double-side polished, 400 μm thick silicon wafer is coated on the front side with a low-stress silicon nitride layer. The SiN is deposited using low pressure chemical vapor deposition (LPCVD). Metal lines are then patterned on the front side of the wafer. Using backside alignment, trenches/vias are patterned in a thick photoresist layer on the backside of the wafer for DRIE. The trenches/vias must be precisely aligned with respect to the front side metal pattern. The DRIE process is then used to etch the silicon and stop on the front side SiN membrane.

The single-step DRIE process did not yield the dimensional accuracy needed for the FPW resonators. Figure 8 shows an optical micrograph of a typical silicon "foot" left behind by the single-step DRIE process. In this particular device the foot is a few hundred microns wide, but not particularly uniform around the perimeter. Typically the foot characteristics are also not uniform across a wafer, making it difficult to compensate for them in the design. The foot can be minimized or eliminated by over etching the feature. This is demonstrated in Figure 8 where the overetch is increased from zero to 25 minutes for a 400 µm deep, 1 mm^2 feature. Unfortunately, as the overetch time is extended the SiN membrane is exposed to the plasma and sputtered etched at a relatively low rate which changes the thickness of the membrane and the functionality of the FPW.

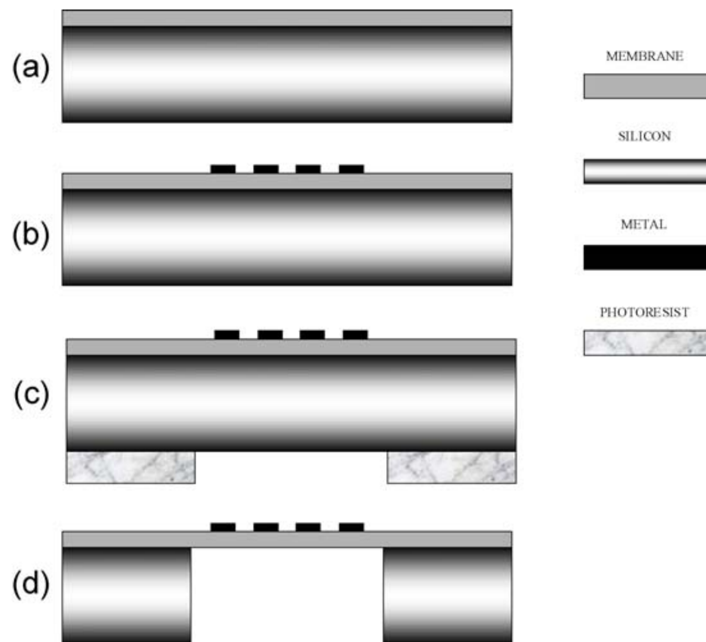

Figure 7. Cross sectional representations of key steps in the fabrication of mag-FPW resonators using a single-step DRIE process. (a) The starting substrate is coated on the front side with low-stress SiN. (b) Metal is patterned on the front side of the wafer. (c) Patterned photoresist defines a window on the backside that is centered with respect to the metal features already defined on the front side. (d) The membrane is released using the DRIE process.

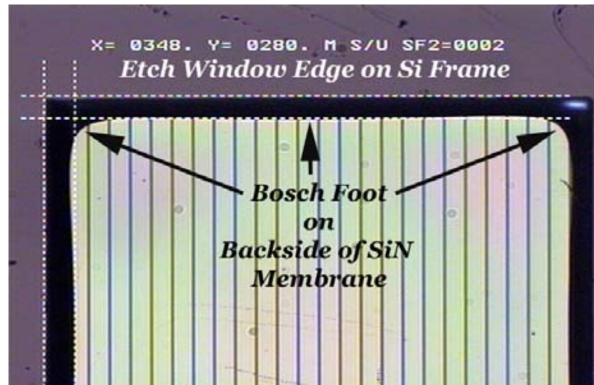

Figure 8. Optical micrograph depicting the typical Si "foot" remaining when a single-step DRIE process is used to release the FPW membrane. The intended edge of the membrane is the outside edge of the darker region.

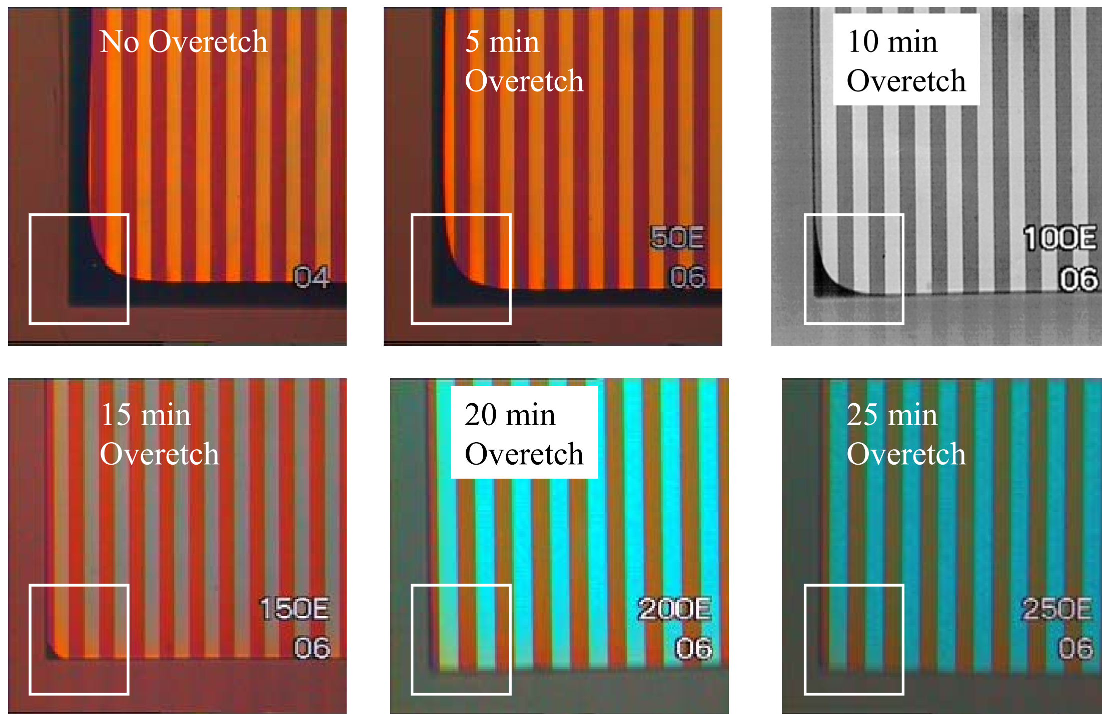

Figure 9. Optical micrographs which show the removal of the Si foot in the corners of the DRIE feature as the overetch time is increased. The SiN membrane is also exposed to the plasma during the overetch period and can thin out due to sputtering of the film.

Since the overetch as well as varying the plasma conditions did not eliminate the Si foot, we developed a multi-step DRIE process that is shown schematically in Figure 10. The additional steps shown in Figure 6 are inserted immediately after step C in Figure 7. In this process the initial mask layer applied to the backside of the wafer is a hard mask. This mask can be a dielectric film, a metal, or a hard-baked photoresist that is resistant to acetone strips. The hard mask is used to pattern the FPW trench/via feature.

Once this hard mask is patterned, a soft mask photoresist layer using conventional photolithography steps is patterned and defines a narrow channel around the perimeter of the FPW trench/via feature. The soft mask protects not only the hard mask, but also the center region of the FPW membrane. The channel is etched using the DRIE process to a defined depth. The soft mask is removed using an acetone rinse that does not attack the hard mask. The DRIE process is then completed to open the FPW trench/via and stops on the SiN membrane. By carefully defining the width of the channel in the mask layout and the channel depth we were able to clear the FPW feature with a significantly reduced Si foot. This process is enabled due to the slower etch rate in the channel as compared to the etch rate in the larger FPW feature and is commonly referred to as aspect ratio dependent etching (ARDE) or RIE lag.

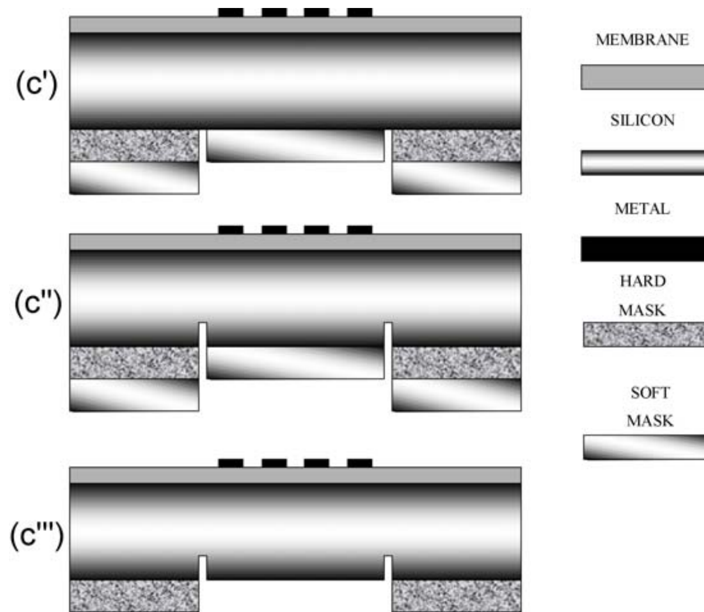

Figure 10. Additional steps used in implementing a multi-step DRIE process that provides vastly improved dimensional control for the FPW membrane. The patterned resist in step C of Figure 2 is hard baked and then protected with a normal soft baked resist that also protects the center region of the membrane etch window. The narrow channel (50µm wide) around the perimeter of the membrane is etched partway into the wafer as depicted in panel c"' (normally about 25% of the wafer thickness). Then the soft mask is stripped and the etch is run until the membrane is released.

An example of ARDE obtained in the DRIE process is shown in Figure 11 for one and 3.5 µm wide trenches. The etch depth for the 1-µm trenches was approximately 7.5 µm while the 3.5 µm trenches were etched to a depth of approximately 9.5 µm. The difference in etch depth is attributed to transport of reactants and etch products into and out of the trenches. As lateral dimensions decrease or the etch depths increase it becomes more difficult for the reactive species to diffuse to the bottom of the trench and more difficult for etch products to be extracted. Improved ARDE effects have been obtained

for the DRIE process under high SF_6 flow conditions due to a reduction in redeposition of etch products.

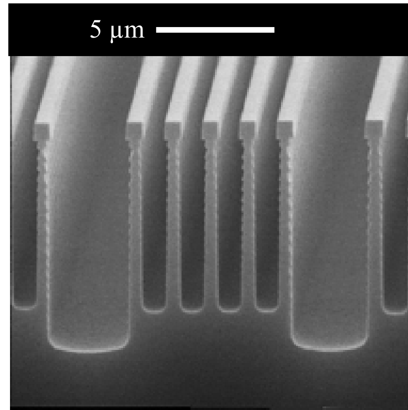

Figure 11. SEM micrograph of Si DRIE etch which demonstrates ARDE. The 1 µm wide trenches were etched to an approximate depth of 7.5 µm while the 3.5 µm trenches were etched to a depth of approximately 9.5 µm.

An example of the multi-step DRIE process is shown in Figure 12. The process used a thermal SiO_2 layer as the hard mask and AZ-4330 photoresist as the soft mask. The channels for all three samples were etched to an initial depth of 100 µm before the soft mask was removed. The channels were 50, 150, and 250 µm wide as defined in the mask layout. The samples were then etched further to a depth of approximately 400 µm using the oxide mask. Notice the channel is still significantly deeper than the larger trench/via feature.

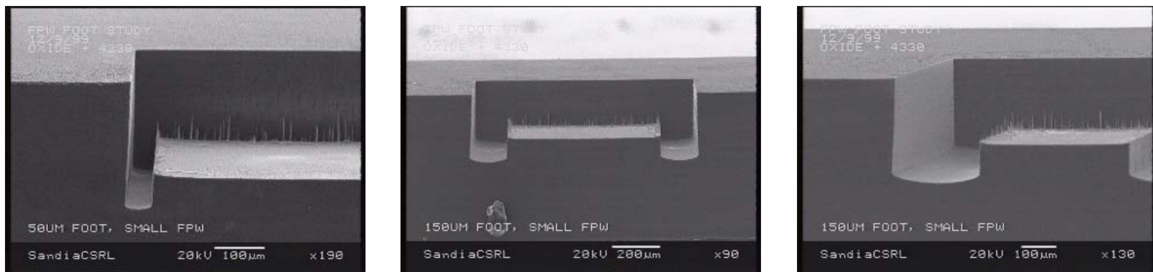

50 µm channel 100 µm deep start | 150 µm channel 100 µm deep start | 250 µm channel 100 µm deep start

Figure 12. SEM micrographs of the multi-step DRIE process. The channels widths were 50, 150, and 250 µm, respectively. Each channel was initially etched to a depth of 100 µm. Following the second etch (to a depth of ~400 µm) the channels were significantly deeper.

In Figure 13, the channel was initially etched to a depth of 50 µm. Notice that following the second DRIE the channel and larger trench/via feature are much closer to the same depth (~400 µm). This process is shown in more detail for a membrane-based device in Figure 9. The DRIE feature was etched to a low-stress SiN film on the front

side of the wafer. A 50 µm wide channel was etched to an initial depth of 80 µm. The DRIE was then completed for a 1-mm^2 feature down to the SiN front side membrane (~ 400 µm deep). Notice a Si foot is not observed, however there is some rounding in the corner of the feature.

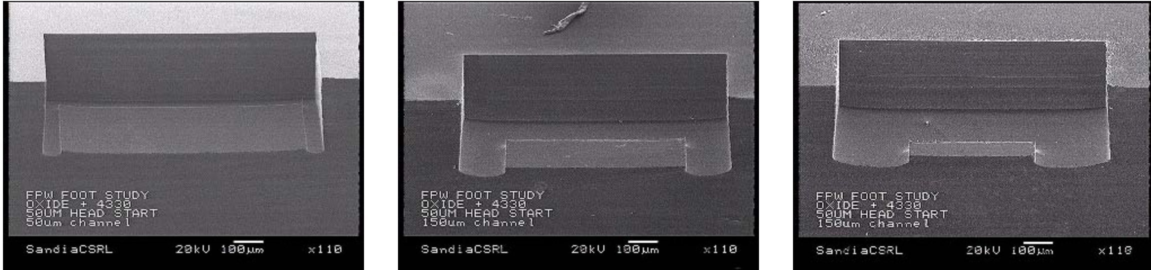

50 µm channel	150 µm channel	250 µm channel
50 µm deep start	50 µm deep start	50 µm deep start

Figure 13. SEM micrographs of the multi-step DRIE process. The channels widths were 50, 150, and 250 µm, respectively. Each channel was initially etched to a depth of 50 µm. Following the second etch (to a depth of ~400 µm) the channels were slightly deeper.

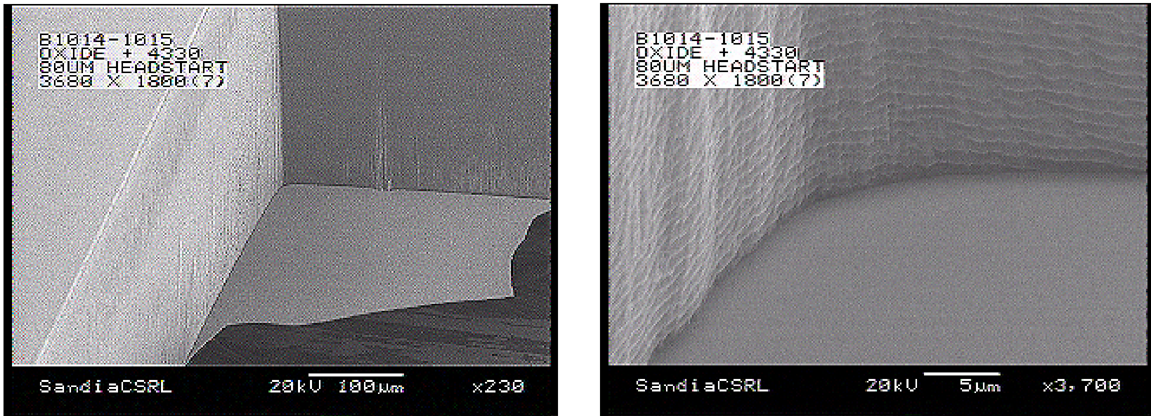

Figure 14. SEM micrographs of the multi-step DRIE process etched to a front side SiN membrane. The channels width was 50 µm and was initially etched to a depth of 80 µm. No Si foot is observed, however some rounding can be seen in the corner under high magnification.

Figure 14 shows that the multi-step DRIE process provides dramatic improvement in the dimensional control of the FPW device. The early DRIE processed devices displayed an irregular silicon foot that might be several hundred microns wide and quite variable across a wafer. The multi-step DRIE process is more repeatable and uniform across a wafer, and results in a regular foot of a few microns (panels (c) and (d) of Figure 10). Figure 15 compares the appearance from the front side of a multi-step DRIE processed FPW resonator with a KOH-etched device. The key thing to notice is the

curvature in the Bosch membrane edge as compared to the KOH membrane edge that is defined by the <111> crystal planes. However, the repeatability, uniformity, and elimination of the silicon foot make it possible to compensate in the mask design for the remaining process-related imperfections.

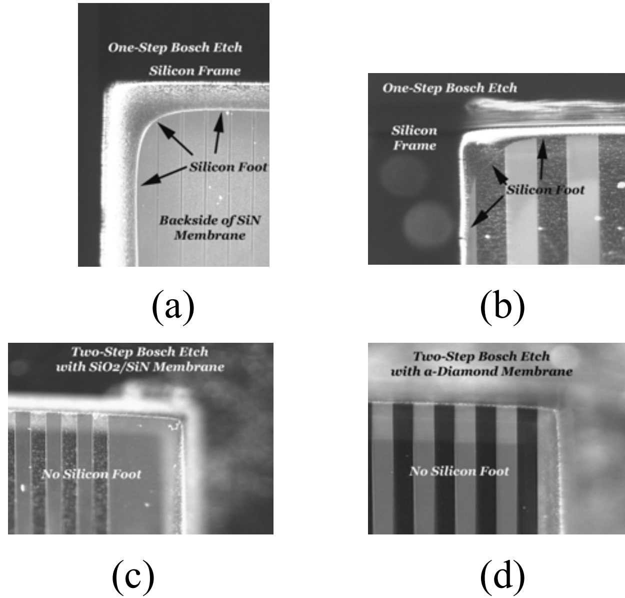

Figure 14. Optical micrographs highlighting the improved control over the silicon foot left behind by the single-step DRIE process. Panels (a) and (b) show typical results with the single-step etch when using SiN membranes. Panels (c) and (d) show the vertical sidewalls achieved with the two-step process, and the lack of a silicon foot. The corners of the membrane are still slightly rounded (25-μm radius is typical) and the edges slightly bowed. The rounded corners are not critical and in principle, the bowed membrane edge can be compensated in the mask design to give a sufficiently straight edge.

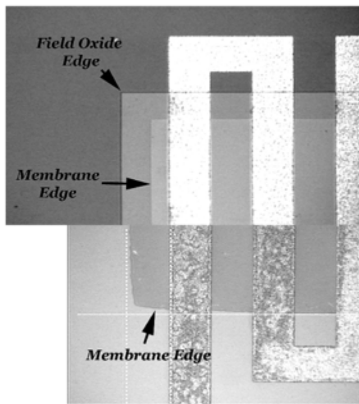

Figure 15. Optical micrographs of the corner of FPW resonator membranes released with either a KOH etch (top panel), or the two-step DRIE etch (lower panel). These pictures are taken from the front side of the membrane (see panels (c) and (d) of Figure 10 for the appearance from the backside of the DRIE-etched membrane).

The same methods used to minimize the Bosch foot around the edge of the FPW membrane can be used to etch multiple depth structures. This was done in the case of the accelerometer structures discussed later in this report.

Characterization Methods

Dimensional Characterization

An optical microscope with a calibrated measurement system was used to determine how well we were able to control the device dimensions with respect to the intended values. Several parameters are of importance in the device operation. Since these are resonator devices, the precise membrane dimensions are of importance. Simple theory suggests the edge dimensions of the membrane should be an integral number of half wavelengths since the silicon frame clamps them. Furthermore, the metal transducer line pattern should be well centered and rotationally aligned within the membrane edges or the acoustic waves reflected from the edges will destructively interfere and one will lose signal strength. Typically we characterized the FPW membrane dimensions as indicated in Fig. 16. The distance from the edge of the membrane to the edge of the outside metal transducer lines was measured at three locations along each end of the FPW. We also measured the metal line width as a check on our lithography. This combination of measurements allowed us to determine if the membranes were the expected size, if the edges were straight or bowed, and if the metal transducer pattern was properly centered and rotationally aligned.

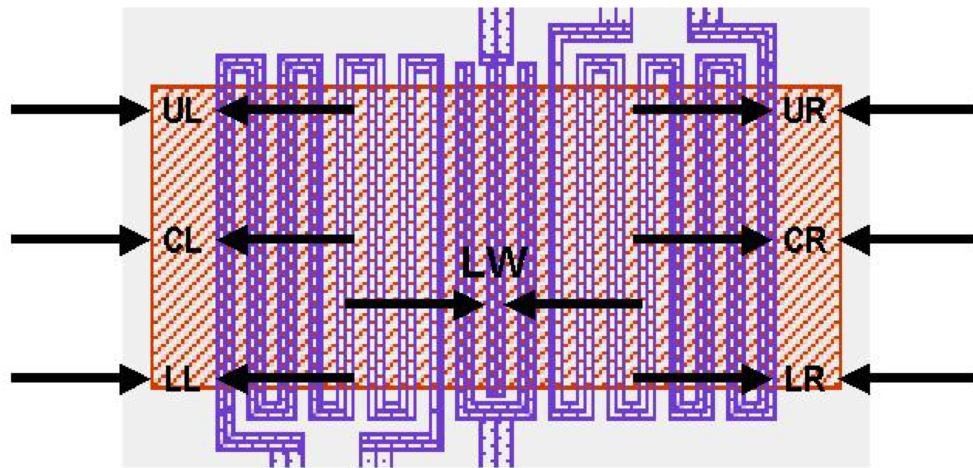

Figure 16. Dimension measurements were made at the indicated locations using an optical microscope. The MLTs are indicated in blue, while the membrane is red.

Network Analysis

In addition to determining optically whether or not we had fabricated FPW devices that matched our design dimensions, we characterized them electrically using a Hewlett-Packard 8751A Network Analyzer. Network analysis allows one to characterize the frequency response of the FPW resonators. The devices are designed to resonate at a particular mode or frequency. The network analysis shows experimentally what frequencies are actually being excited, and at what relative strengths. These are

correlated to the device design, imperfections, and drive configuration. Both two-port and one-port devices were routinely characterized using a Hewlett-Packard 8751A network analyzer. Reflection measurements were used to characterize the single-port devices because the same port is used to excite and detect the FPW. This also turned out to be a useful characterization technique for characterizing individual input and output transducers on two-port devices. Transmission measurements were used to characterize true two-port operation.

Mode Imaging

While network analysis could tell what the resonant frequencies were experimentally, one cannot know precisely what mode is being excited without actually imaging it. One of the unique capabilities that Sandia has developed as part of this investigation is the ability to image surface oscillations of FPW devices using a laser based synchronous microscopy system. This is accomplished by focusing a collimated HeNe laser beam to a $\leq$ 10-μm spot on the surface of the FPW. The reflected light is projected onto a FIL-C10D silicon photodiode manufactured by UDT Sensors Inc. A 1-μradian change in the slope of the FPW surface causes about a 100-nA change in the output signal of the photodiode. A two-channel phase-lock amplifier based on the Analog Devices AD630 Balanced Modulator/Demodulator chip was built to measure these small-amplitude, high frequency signals at the driving frequency of the FPW. The spot is scanned over the surface of the FPW to measure the slope at selected intervals. Scanning

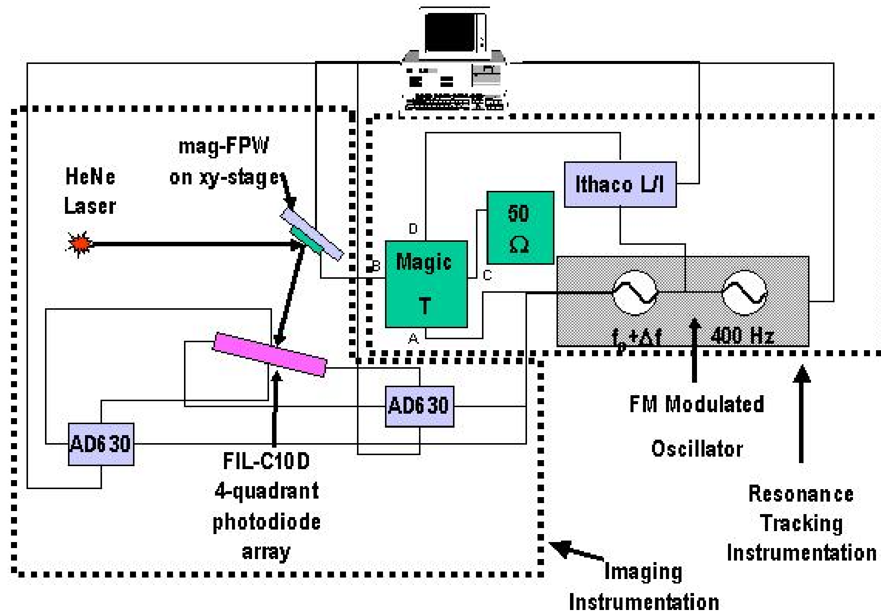

Figure 17. Schematic diagram of the mode imaging system used to identify resonant modes excited in the FPW resonators. The system included the capability to track a resonant peak because heating due to the laser beam caused enough temperature shift to cause the resonant frequency to change.

at 20-μm x 20-μm intervals requires about one hour to acquire an image of the surface

slope. The resulting profile can be integrated along the surface to produce a topographical map showing the mode structure. However, we generally just used the slope image.

FPW devices are extremely sensitive to temperature changes; a 1°C increase in temperature can cause a 2 kHz decrease in resonant frequency. Heating from the laser and changes in ambient conditions cause the resonant frequency to drift during the imaging process. To avoid getting out of resonance during the time it takes to acquire a mode image, a tracking system was used to lock-in on the impedance shift associated with resonant mode structures. An impedance sweep was performed prior to imaging the device, and the system was locked on the peak of interest. In order to identify and track individual peaks an HP function generator is used to drive the FPW device through an RF circulator (also called a Magic T in Fig. 17). The signal passing through the circulator to port D depends upon the relative balance between the FPW impedance on port B and the 50-ohm load on port C of the circulator. (In principle, if the FPW impedance were 50 ohms, no power would be seen at port D.) In order to pick up small changes in the transmitted power, we modulate the drive frequency at 400 Hz with a 200 Hz amplitude. That is for example, when the drive frequency is set to 400 kHz, the actual drive frequency varies at 400 Hz sinusoidally from 400 kHz – 100 Hz to 400 kHz + 100 Hz. An Ithaco lock-in amplifier is used to monitor the power passed through the circulator. The reference channel of the lock-in is the 400 Hz signal used to modulate the drive frequency. When the drive frequency passes through a resonant frequency of the device, the impedance balance between the FPW and the 50-ohm load starts to vary significantly (at the 400 Hz reference or modulation frequency). Thus the Ithaco lock-in measures the derivative of the FPW frequency response curve. A LabView program was written to measure this derivative response curve, and then allow one to pick a particular zero crossing (i.e. resonance peak) to track.

While tracking the resonant peak, a second LabView module monitors the output of the AD630 demodulator chip, which is measuring the surface slope variations occurring at the drive frequency.

Modeling

A finite element model (FEM) of the FPW was developed using Structural Research & Analysis Corporation's COSMOS/M FEM package with the Advanced Dynamic Module for the dynamic portion of the analysis. The analysis was conducted by first solving for the eigenmodes of a pre-stressed membrane, and then solving for the selement displacements induced by an oscillating normal pressure load imposed along the transducer lines. The FPW was modeled using layered shell elements where one layer is the membrane, and the second layer is the transducer line. All six degrees of freedom were locked along the edges of the membrane in this model. A pre-stress was created in the membrane by performing a thermal analysis where the membrane cools from an unstressed elevated temperature. Tensile stresses in the silicon-nitride films have been measured to be between 80 MPa and 230 MPa[24]. Measurements made on one device showed that the membrane tension was around 228 MPa (see appendix A), however, tension will vary with wafer processing and operating temperature. For most of the devices tested, the membrane tension appeared to be closer to 150 MPa.

The effective load along the transducer lines can be calculated using Lorentz's equation for force on a conductor in a magnetic field[25]. If B is the magnetic field strength, and I is the current in the conductor perpendicular to the field, then the force over a unit length, δL, is given as $F = B\ I\ \delta L$. For a conductor of width w, the effective normal pressure load on the conductor is

$$P = \frac{B\ I}{w}\ . \tag{19}$$

Typically, the magnetic field strength is around 0.4 Tesla (1 Tesla = 1 N/A m), and the current through a single transducer line is around 100 μA, so the induced load on a 100 μm wide, transducer line is on the order of 0.4 Pa.

In the case of an oscillating current, the electromagnetic forces place an oscillating load on the membrane. To solve for the displacement of the membrane, the COSMOS/M Advanced Dynamic Module solves the equations of motion for a linear dynamic system given by the equation of motion,

$$[M]\{\ddot{u}\} + [C]\{\dot{u}\} + [K]\{u\} = \{f(t)\} \tag{20}$$

where $[M]$ is the mass matrix for the finite element system, $[C]$ is the dampening matrix, $[K]$ is the stiffness matrix, $\{u\}$ is the displacement vector and $\{f(t)\}$ is the time varying force vector[26]. COSMOS/M solves Eq. 20 by the method of modal analysis; Eq. 20 is broken into a series of uncoupled second order differential equations using the eigenvectors (modal shapes) and eigenvalues (natural frequencies) of the undamped finite element system of equations. The resulting linear system of differential equations that describe the damped, forced vibrations of the membrane are then solved to determine the relative contribution of each fundamental mode structure (eigenvector) to the displacement matrix. The final deformed shape of the membrane is a composite of all of the mode structures up to and beyond the driving frequency of the system[27]. COSMOS/M offers several options to model damping in the system. For this analysis, a modal damping was selected with a damping coefficient of one-half of one percent of critical damping for each natural mode shape.

General Characterization Results for FPW resonators

Higher Order Resonators

KOH-Etched Devices

As mentioned in the earlier sections, the simple model predicts that dimensionally perfect devices to provide the best performance. Devices were designed so that the center of the outermost transducer lines were exactly a quarter wavelength from the edge of the membrane. It was also important to make sure that the edges of the membrane were precisely straight, and that the transducer lines were exactly parallel to the reflector edges. The general approach was that the frequency response of a dimensionally perfect device should show a single dominant mode with perhaps some weaker modes due to additional transverse modes.

Our earliest devices, processed using the wet anisotropic etch to release the membrane, were anything but perfect. The membranes were grossly oversized (hundreds of microns on a membrane of a few thousand microns) and had jagged edges because they were not perfectly aligned to the 110 directions. The devices also suffered from rotational misalignment of the MLTs with respect to the membrane edges. In spite of these imperfections, some of the early devices displayed quite reasonable performance (see Fig. 18). Note that the frequency response shows several different modes could be excited with nearly equal strength. We assumed that improvement in the process control would improve the dimensional characteristics and solve many of these problems, and that perfect devices would have much improved performance.

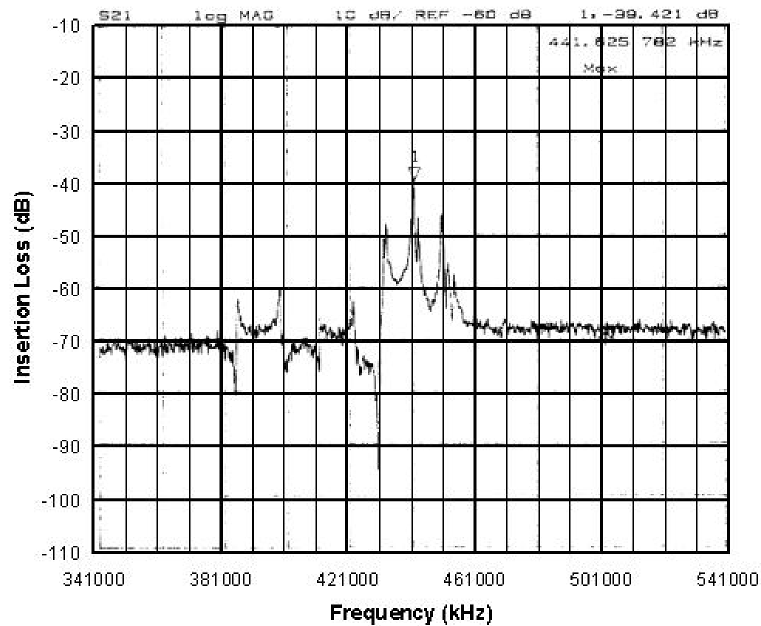

Figure 18. Broadband frequency scan of an early mag-FPW resonator with poor dimensional characteristics.

After spending considerable time improving the wet anisotropic etch processing protocol, we were able to consistently produce FPW resonators with near perfect

dimensional control. To our surprise, the performance of the most dimensionally perfect devices was not improved, and in some ways even inferior to the early devices with sloppy dimensional control. This result launched us on a study of the effects of membrane size. During the course of these measurements we also learned that the additional modes seen even in our "perfect" two-port devices were caused at least partially by the two-port drive configuration where not all of the transducer legs on the membrane are driven. All of this was determined through dimensional characterization, combined with network analysis and mode imaging as a function of membrane size and drive configuration. The general design principles that grew out of this work are summarized below, without going into all of the details.

Effects of dimensions on performance

Photomasks for the FPW resonators were designed with 14-µm increments in the membrane size. This produced on a single wafer membrane sizes that would bracket the supposed ideal dimensions, some being too small, others just about right, and still others too large. In addition, designs were include that used 5λ/4 edge spacing in addition to the standard λ/4 design. The hope was that the additional space allowed at the reflector ends of the resonator might make the performance less sensitive to dimensional imperfections.

Figure 19 shows a series of frequency response curves for FPW resonators with nominally λ/4 edge spacing, where the membrane size is intentionally varied from just below ideal, to greater than the ideal value. These are 6N, λ/4 devices that are 14 µm under, ideal, and 14µm oversized. The graphs show not only the traditional two-port transmission response (i.e. S_{21}) , but also the single-port reflection response measured when driving either the input port (S_{11}) or the output port (S_{22}). The reflection response has been converted to units of impedance.

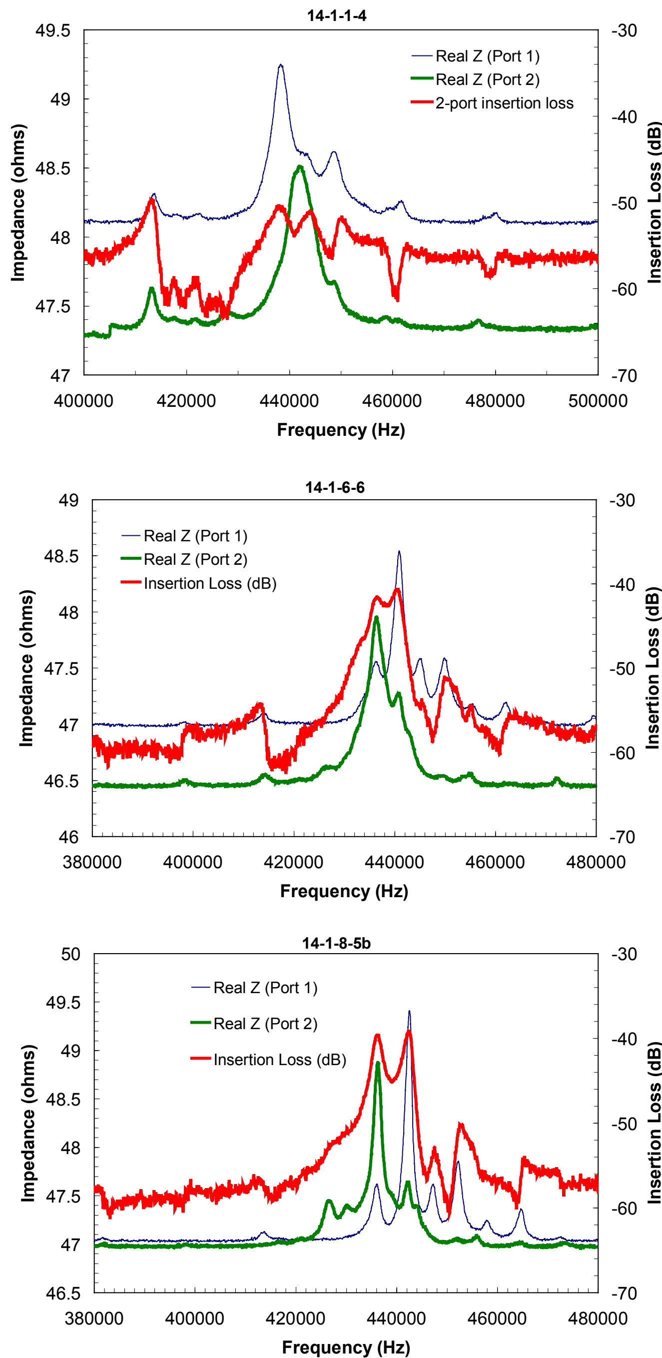

Figure 19. These three panels show (from top to bottom) the effects of variation in the

membrane size about the ideal. In the top panel, the membrane is about 14 μm undersized. In the middle panel the membrane is the ideal size. In the lower panel the membrane is 14 μm too large. These devices have a wavelength of 320 μm, with 12 transducer legs in each port, and three grounded dummy legs separating the input and output ports (these legs are used to cut down the direct feedthrough). The blue and green traces indicate the impedance indicated by a reflection measurement done on the input or output port. The red trace is the traditional two-port transmission response.

In each one-port response curve, one can clearly see a number of resonant modes, with one dominant mode. However, the dominant mode for the input port does not match the dominant mode for the output port on any of the three devices. With the undersized membrane, the major peaks seen when driving the input or output ports tend to be a bit broader and they slightly overlap. This leads to a weak two-port transmission response shown by the red trace in the top panel. As the membrane size increases the major peak for each port tends to sharpen up a bit, and a minor peak is resolved that is a frequency match for the major peak excited by the other port. This leads to a relative strong two-port transmission response with two major peaks. The two major peaks tend to separate in frequency as the membrane size increases.

Figure 20 shows the effects of adding an additional full wavelength to each end of the resonator membrane. The single-port response of each port shows two major peaks, plus several smaller peaks. Note that there is a good frequency match of the major peaks excited by the two ports, even though the amplitudes are not necessarily the same. Note also that the two major peaks have separated more in frequency compared to the λ/4 device in the middle panel of Fig. 19. The increased separation makes the device easier to use as a sensor because it reduces the amount of mode hopping that can occur when trying t ... rength modes.

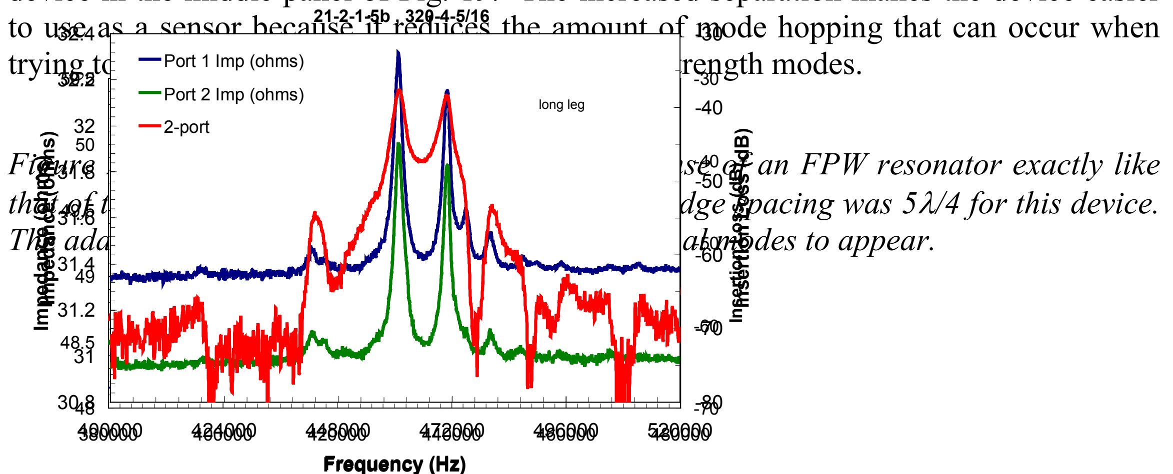

Figure ... se of an FPW resonator exactly like that of t ... dge spacing was 5λ/4 for this device. The add ... al modes to appear.

Figure 21. This graph shows the frequency response of a device from a later lot that used the same parameters as the devices of Fig. 19, except that a 5λ/16 edge spacing was used. The general shape of the frequency response fits the trends with membrane size discussed above.

Rather than increase the membrane size by a full wavelength on each end, we found that it was effective to add only about an extra sixteenth of a wavelength on each end (i.e. λ/8 to the whole membrane), leaving the edge spacing at 5λ/16. The frequency response of such a device is shown in Fig. 21, and it fits the trends with respect to membrane size discussed above.

This device has one other difference from the devices of Fig. 19 which we found to be useful. This device has lower baseline impedance of the transducers (achieved by using thicker aluminum metalization). We found that lower impedance improved the two port response by lowering the baseline insertion loss. The decrease from about 45 ohms in Fig. 19, to 30 ohms in Fig. 21 lowered the baseline insertion loss about 10 dB. As a general rule of thumb, we found that the lower the transducer impedance the better. This ran contrary to our initial inclination to build 50-ohm devices for easier matching with the drive circuitry.

Studies were also conducted to determine the best number of legs to use in the transducers. When the early devices were found to have so many modes, it was felt that more legs would help to control the mode structure better. Devices with as few as four, and as many as 12 legs/transducer, were tested. A good compromise based on performance and membrane size seemed to be about 8 legs/transducer for two-port devices, and this design was used for later applications.

As mentioned above, we found that the frequency response of the FPW resonators depended strongly on the drive configuration. In a typical single port device, all of the legs are driven. This results in a clean frequency response spectum showing the dominant design mode plus a family of weaker additional modes presumably arising from the additional transverse modes. An example of this behavior is seen in Fig. 22. This device was a 10-legged single-port FPW resonator with a wavelength of 640 μm. However, there were additional transducer taps (see the inset picture in the top panel of Fig. 22) so that varying combinations of the transducer legs could be driven. In this way we could drive all 10 legs (normal for a single port device) or drive just the legs (1-4 in this case) that would correspond to the input port of a two-port resonator of identical dimensions. The blue trace in the top panel shows the classic expected response when all ten legs are driven. The single large peak in this case is expected to be the 10-1 mode, while the smaller amplitude peaks at higher frequencies correspond to the 10-3 and 10-5 modes (these mode identifications were verified with mode imaging experiments discussed below). Note that when only the four legs are driven (corresponding to the input port legs of an equivalent two-port device) additional peaks show up in addition to the intended 10-1 mode. When this is compared to the two-port device frequency response shown in the lower panel of Fig. 22, the similarities are obvious.

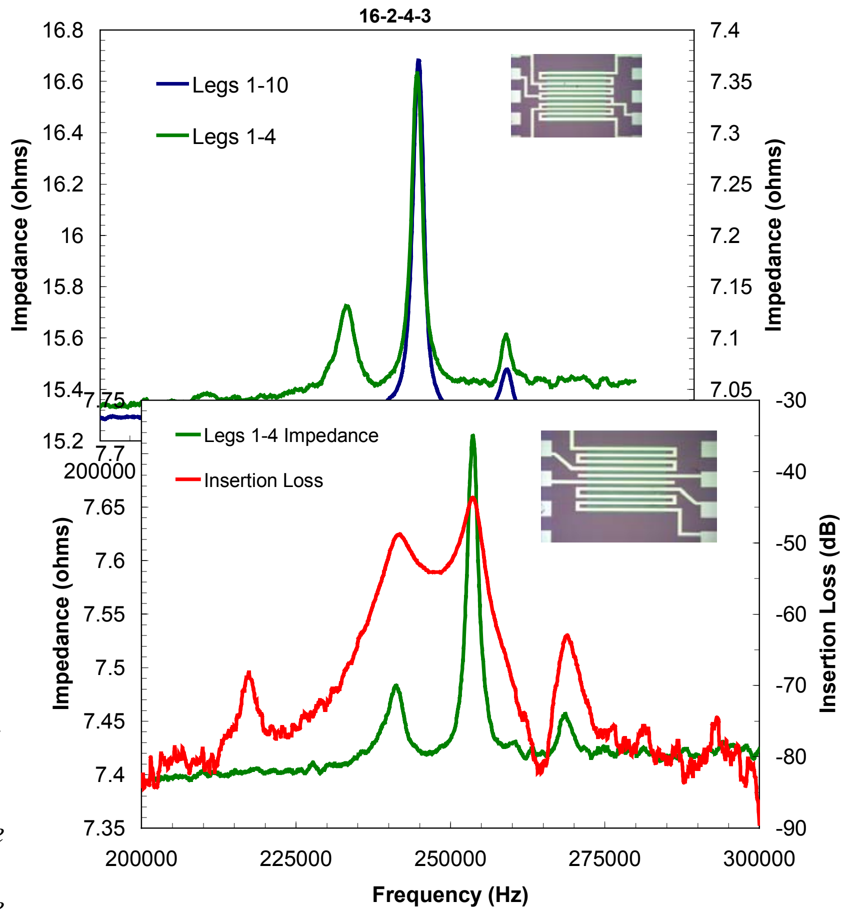

Figure 22. The upper panel shows the frequency response of a single port FPW resonator when all legs are driven, and when only the first four legs on one end of the membrane are driven. The device has a wavelength of 640 μm, 10 legs in the MLT, and a λ/4 edge spacing. The inset shows the single port MLT layout that allows one to drive various combinations of the legs. When all ten legs are driven one observes a dominant mode, followed at higher frequencies by a family of progressively lower amplitude modes, in agreement with the theory discussed earlier in this report. When only the first four legs are driven, additional strong modes appear at both lower and higher frequencies. The lower panel shows the frequency response of a twin two-port device that has the same physical dimensions, but has four legs in the input and output MLTs, separated by two grounded dummy legs. Note the similar impedance response to that in the upper panel when only the first four legs were driven. The red trace shows the familiar S_{21} response for the two-port resonators.

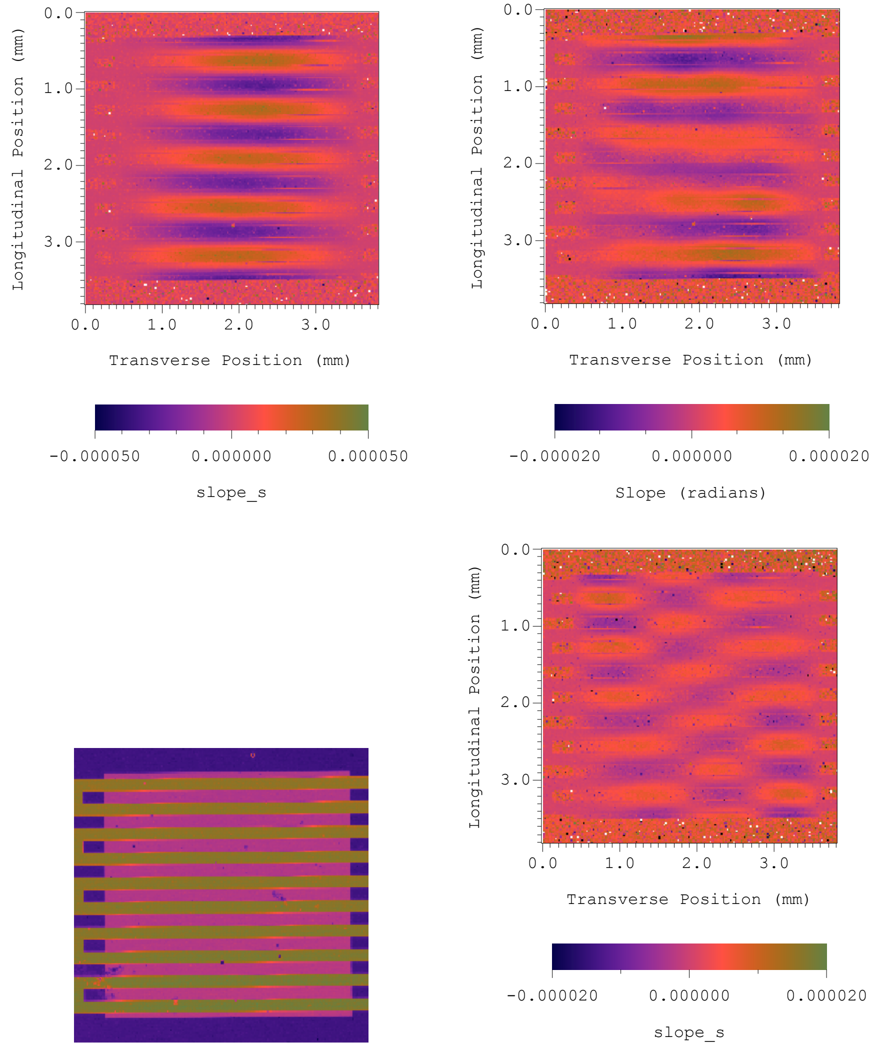

Figure 23. Mode images of the surface slope taken from the device whose frequency response is shown in the upper panel of Fig. 22. The upper left panel is the surface slope image obtained when all 10 transducer lines are driven at the frequency corresponding to the largest peak (about 253 kHz) in the upper panel of Fig. 22. There are 11 slope maxima along the longitudinal axis, corresponding to a 10 X 1 mode. The surface slope image in the upper right hand panel was measured while driving only legs one through four in the lower half of the membrane, at the lower frequency peak (about 242 kHz) in Fig. 22. Notice that there is one less longitudinal slope maxima, thus the image corresponds to a 9 X 1 mode. The image in the lower right was taken driving all 10 TLs at the higher frequency peak (about 267 kHz) shown in Fig. 22. This image corresponds to a 10 X 3 mode. The lower right image shows the layout of the FPW during the imaging experiments. The tranducer lines, membrane, and silicon frame appear yellow, pink, and purple respectively in this false color image.

The remaining piece of the puzzle was to positively identify the various modes that appear under the different drive configurations. Figure 23 shows mode images

collected under the same drive configurations as discussed in the upper panel of Fig. 22. The mode images corroborate the discussion above.

In devices with more legs in the transducers, these additional nodes tended to be closer in frequency than in the devices with few legs. That is, in devices with the same transducer wavelength (and the same nominal resonant frequency), the frequency difference between the 10-1 and 9-1 modes on a 10-legged device was larger than the difference in frequency between the 19-1 and 18-1 modes in the 19-legged device. We also found that it was easier to excite the modes with too few or too many antinodes in the devices with larger edge spacing (5λ/4 as versus λ/4).

In addition to experimentally imaging the modes, extensive FEA simulations were performed for two test FPW devices corresponding to the types of devices discussed in Figs. 19–23. One was a single-port device with ten transducer lines (TLs), and the other was a two-port device with 19 transducer lines. The modeling parameters were chosen to match those of the actual devices. The single-port device (like that depicted in the upper panel of Fig. 22) was made with a 3.2-mm square silicon nitride membrane that was 0.62-μm thick. Ten aluminum TLs were deposited on the membrane to create a system with a wavelength, λ, of 640 μm. The transducer lines are 160-μm wide (λ/4) and 0.65-μm thick and they were spaced 160 μm apart. The outside edge of the outside TLs are 80 μm from the edge of the membrane. All ten transducer lines can simultaneously drive the FPW, or several combinations of edge and interior TLs can be driven separately. Based on properties in the MEMS database[24] Young's modulus for silicon nitride is 385 GPa, Poison's ratio is 0.27, and the density is 3100 kg/m^3. For aluminum, Young's modulus is 73 GPa, Poison's ratio is 0.3, and the density is 2768 kg/m^3 [28]. A prestress of 150 MPa was introduced in the membrane by applying a static differential thermal contraction in the model.

The finite element model was used to determine both the structure and amplitude of the vibrating membrane. When the FPW is driven by a 660 μA alternating current in a 0.48 T field, the TLs apply a 2 Pa load on the membrane according to Eq. 19. The displacement of the membrane at Points A, B, and C in Fig. 24 is shown as a function of the driving frequency. A peak displacement amplitude of 118 Å occurs at the center of the TLs when all ten transducers are driven with a 264-kHz, 660-μA alternating current. This peak corresponds with the 10x1 mode described above. The minor hump (~50Å) that is observed around 274 kHz corresponds to the 10x3 mode shape and the 20 Å peak at 294 kHz occurs when the 10x5 mode is excited. In general, it is desirable to have discrete mode structures with a wide frequency spacing between adjacent modes. This characteristic makes it easier to track the impedance output of the FPW device.

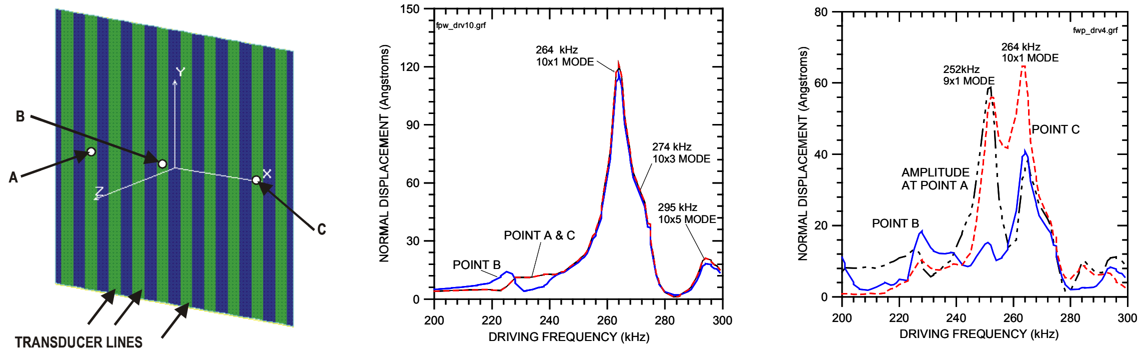

Figure 24. Surface-normal displacement of FPW at three locations. . Points A, B, and C are at the center of the transducer lines (TLs). Center figure shows displacement driving all 10 TLs. Right figure shows displacement driving left-four TLs.

When driving all ten TLs, there is uniformity in displacements on the FPW surface, as might be expected. In the two-port drive configuration (only a portion of the TLs is driven, and the remaining lines are used as the output transducer or dummy lines for noise reduction) uniformity is lost and maximum displacement peaks can occur at frequencies where natural modes are combined. The right panel of Figure 24 shows the displacement at Points A, B, and C when the FPW is driven with the four left-most transducer lines. Once again, the dominant peak occurs at 264 kHz when the 10x1 mode shape is excited with the 660-μA current. The maximum displacement, however, is about 50% higher on the undriven side of the FPW (65 Å on the undriven side compared to 37 Å on the driven side). Between 252 and 264 kHz the displacement amplitudes of the membrane remain relatively high as the membrane transforms from a 9x1 mode structure to a 10x1 mode structure. Figure 25 shows the shape of the membrane at a driving frequency between these two fundamental modes. At this frequency, the higher amplitudes actually occur on the undriven transducers; peak displacement amplitudes will lead to peak induced currents on the right-four TLs. It is the induced current that is used to monitor resonance behavior in FPWs.

In addition to studying the effects of how the FPW is driven, several other parameters were studied with the FEA model. The FPW pictured in Fig. 24 with all ten transducer lines driven was used as the standard for these parametric studies. The amplitude of vibration was found to be proportional to the magnitude of the driving current, as would be expected for a linear elastic FEM formulation. (It is reported, however, that stiffening occurs for larger amplitude driving currents, because large displacement amplitudes begin to induce stresses comparable to the membrane pretension.[6]) The FEM model also predicts that doubling the electrode thickness from 0.65 μm to 1.30 μm decreases the 10x1 mode excitation frequency from 264 kHz to 229 kHz, while the peak displacement amplitude only declines by about 5%. When the spacing between the edge of the transducer lines and the edge of the membrane increases from 80 μm to 100 μm (this is a λ /32 increase from the expected optimum spacing of $\lambda/4$), the maximum displacement amplitude increases by 3% and the frequency needed to excite the 10x1 mode decreases to 261 kHz. If the TLs are offset by 20-μm from the

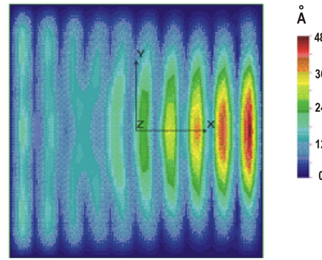

Figure 25. Predicted mode structure at 258 kHz when the FPW in Fig. 23 is driven by the left four transducer lines. This structure occurs between the 9x1 mode and the 10x1 mode shown in Fig. 24.

center of the membrane, then the peak displacement amplitude increases on the side with the wider edge spacing by about 25%, and the peak decreases by about 50% on the side with the narrower edge spacing. This stands in contrast with results from perfectly centered electrodes where displacement amplitudes are nearly uniform across the membrane for the 10x1 mode. It is likely that a 20-μm location error could significantly impact the impedance shift experienced at resonant frequencies.

Above, the results show the displacement of selected points on the surface that result from Lorentz forces on the driving TLs. To more accurately represent the phenomena that generates the device impedance measured in experiments, the model was modified to give the integrated effect of displacement along the entire TL path. The improved model was used to further explore operating characteristics caused by fabrication flaws, packaging loads, and drive approaches. A 1-μm thick silicon nitride membrane and 19-TLs were used in these studies. Model parameters were used to match the actual 19-legged device depicted in Fig. 21. The test device had a 320-micron wavelength and 80-micron wide TLs made of 0.75-micron thick aluminum. Figure 26 shows how a small packaging load on the FPW frame, can result in anomalies in FPW operation. Whether the loading increases or decreases the signal strength depends on how the device is driven according to the model. The model also showed that small loads can actually alter which modes are preferentially excited by the drive electronics. Further modeling showed that making the FPW windows slightly wider than an exact number of wavelengths ($5\lambda/16$ edge spacing rather than $\lambda/4$)) can compensate for misaligned TLs and improve performance. This agrees with the behavior observed on actual devices.

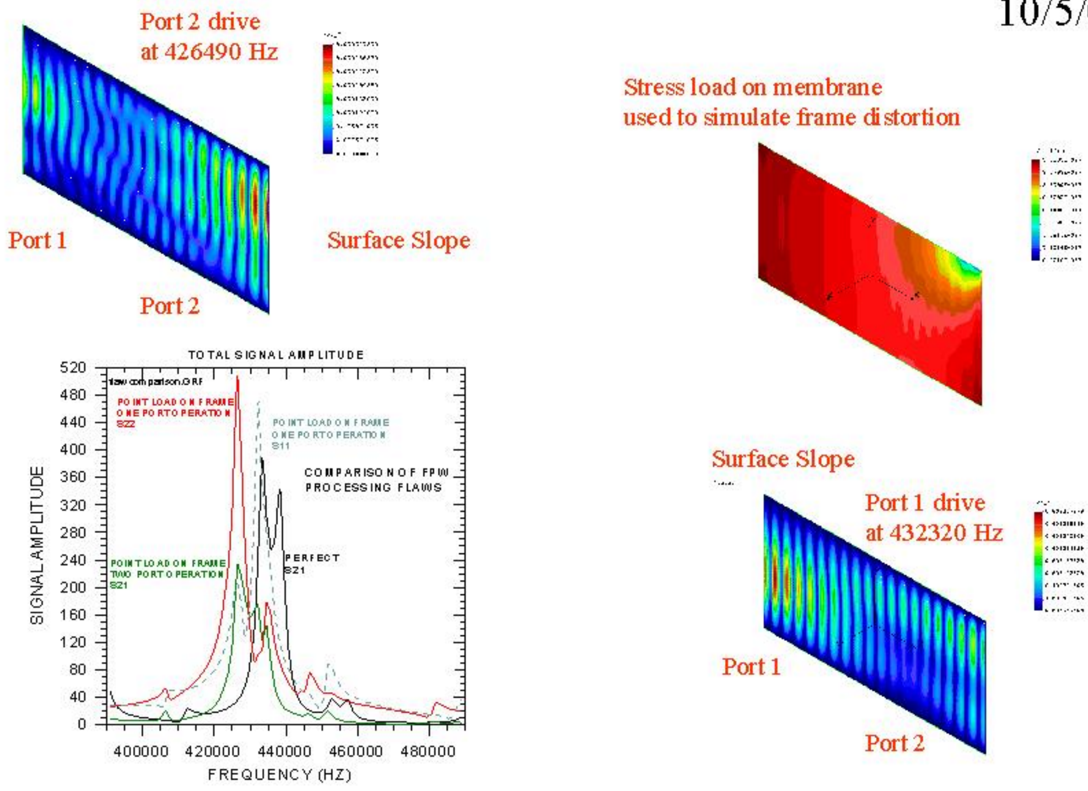

(a)

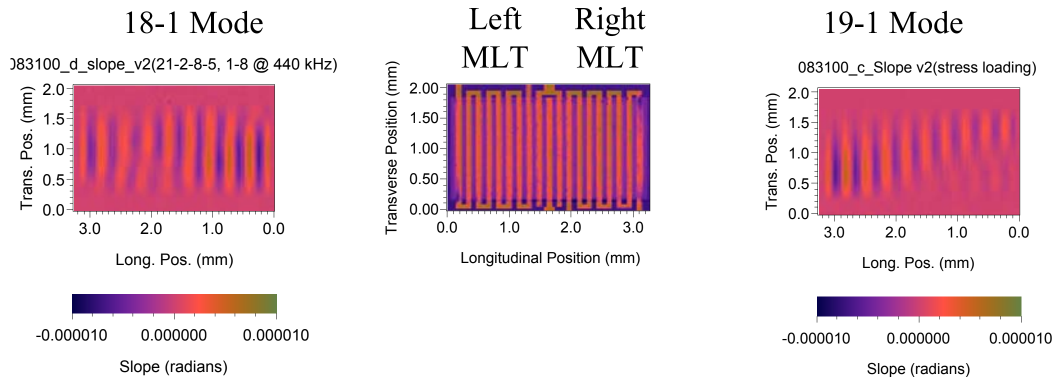

(b)

Figure 26. Model results for an FPW with 19 TLs. Partial loading on the frame is predicted to alter which modes dominate, and also distorts the modes shapes. Panel (a) depicts the FEA results for a perfectly dimensioned two-port device driven with either the left or right meander line transducer (MLT). In addition, a small amount of stress loading is applied to the upper right corner of the membrane for some of the calculations. The frequency response graph shows the effects of the loading and the calculated surface slope graphs show the different dominant modes depending on which MLT was driven. Panel (b) showed the experimentally measured surface slope images for the real device emulated by the FEA model. Qualitative similarities are seen between the calculated and measured surface slope images.

DRIE Processed FPW Resonators

The vast majority of our early FPW development work was done on KOH-etched devices. However, FPW devices are more easily post-processed on wafers with drive electronics when the DRIE protocol is used. Unlike the KOH-etched devices, the reflector edge of the typical DRIE device is not perfectly straight. Fig. 15 (from the earlier design section on DRIE devices) shows typical results for the dimensional characteristics of DRIE devices, achieved after considerable process development (see the earlier section on DRIE processing of FPW resonators).

Figure 27 shows the effects of membrane size on membrane dimensional accuracy when using the DRIE protocol. Clearly RIE lag is affecting the dimensional accuracy. One could presumably compensate for this effect if it is sufficiently repeatable and uniform (across a wafer).

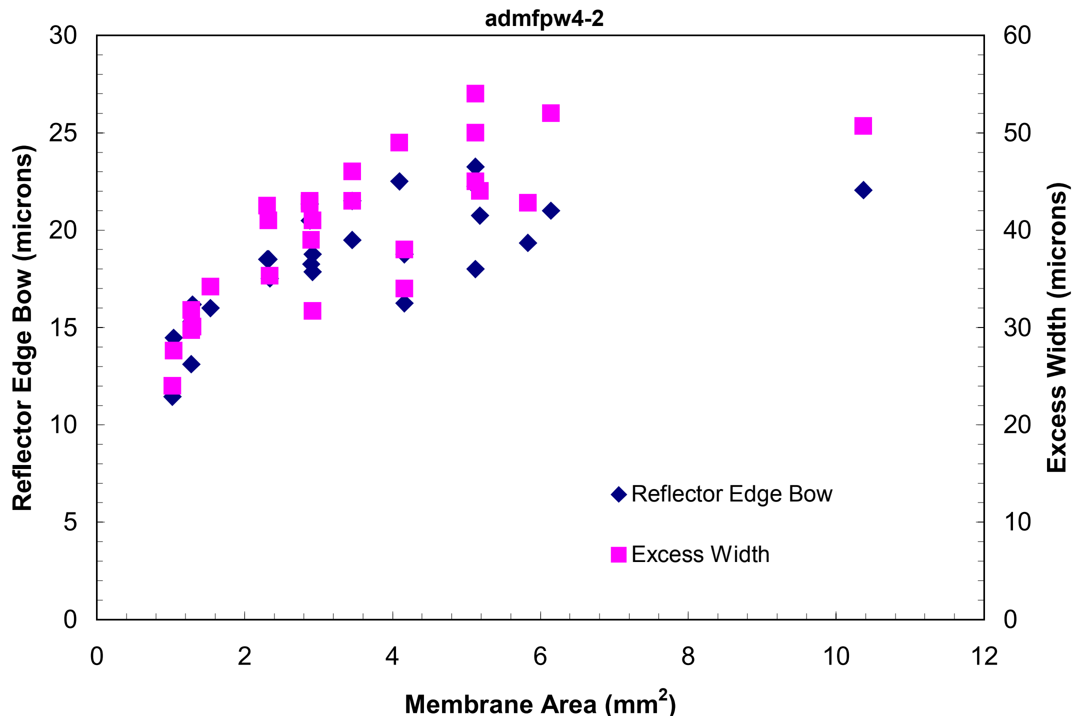

Figure 27. This graph shows the curveature (bow) in the reflector edges of the FPW, and the excess width of the FPW membrane (above the designed width) as a function of membrane area. The membrane dimensions range from nominally 1.2-mm x 0.8 mm to 3.24-mm x 3.2 mm. This dependence upon the area (and even the aspect ratio of the membrane in the smaller devices) arises from the RIE lag effects discussed above. Presumably, one could compensate for these areas in the device design if the uniformity across a wafer is adequate and the effect is repeatable.

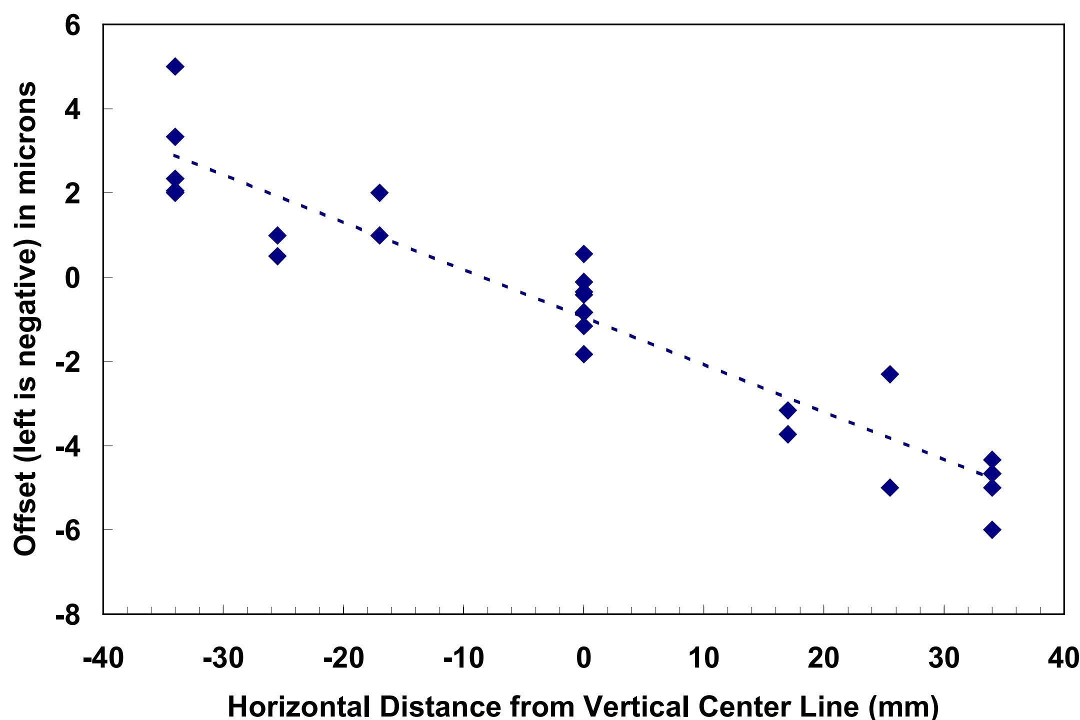

Figure 28. This graph shows the lateral offset of the transducer pattern on DRIE etched FPW resonators from a single wafer. Zero offset would be perfectly centered. This error across the wafer appeared in all DRIE wafers, but was not always the same magnitude. This is actually not a large error (less than 1% of the membrane longitudinal dimension), but it does affect the device performance.

While the membrane size and edge curvature did not appear to be position dependent across the wafer, we did observe a position dependent offset of the transducers with respect to the membrane. This is shown in Figure 28 which indicates transducer placement accuracy as a function of position across the 100-mm wafer.

In spite of these shortcomings, we found that the DRIE FPW resonators could have performance characteristics rivaling that of KOH-etch devices with more ideal dimensional characteristics. Figure 29 shows the frequency response of an FPW resonator made with a 0.28-μm thick amorphous diamond membrane with 0.75-μm thick aluminum metalization. This device had a 320-μm wavelength, 19 legs, and nominally 5λ/16 edge spacing. Actually, the edges were bowed about 15 μm, the edge spacing turned out to be more like 3λ/8, and the transducers are offset one way by about 4 μm. Even so, the resonator characteristics rival those of the best SiN-based FPWs made using the KOH-etching process. Note also, that there is an additional, reasonably strong peak at lower frequencies.

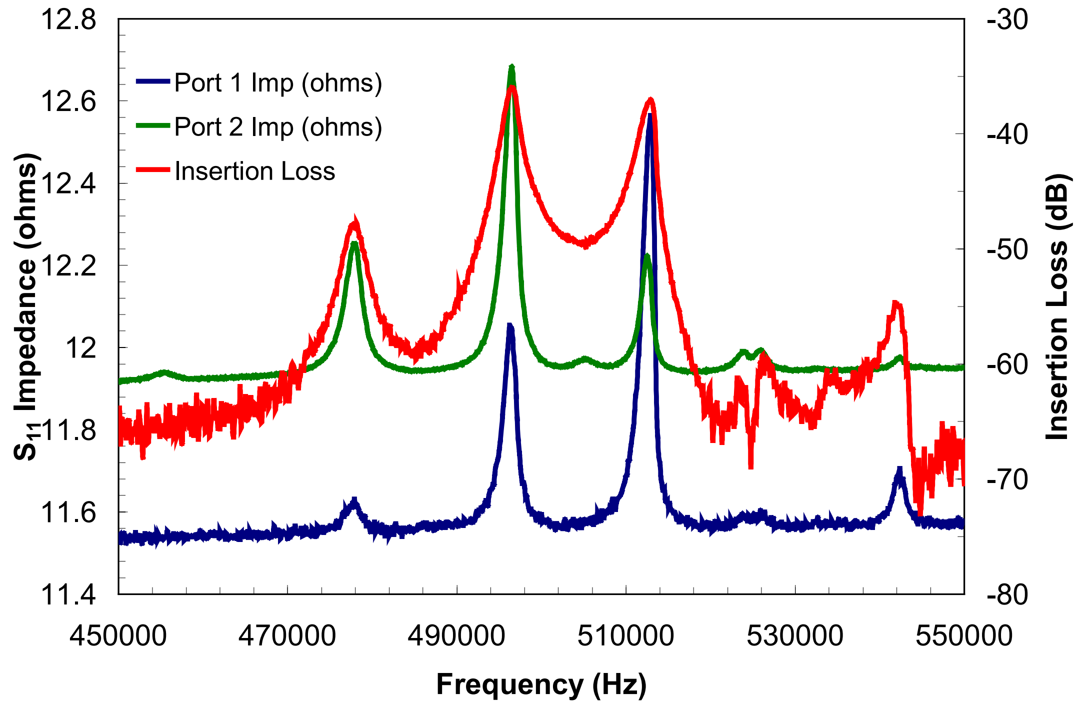

Figure 29. The frequency response of a DRIE processed FPW resonator with a 0.29-μm thick amorphous diamond membrane. The device is a standard configuration that is the same as the nitride FPW from Fig. 21. However, the actual edge spacing turned out to be closer to 3λ /8 and the edges have a 15 -μm bow. A third major peak shows up in this device at lower frequencies due to the oversized membrane.

All of the performance characteristics of the DRIE processed FPWs are consistent with the FEA discussed above. In addition, the bowed edges and rounded corners characteristic of the DRIE devices were modeled, and shown not to be significant problems. The main issue with the DRIE devices will be to achieve repeatable and uniform characteristics across a wafer.

Device Image

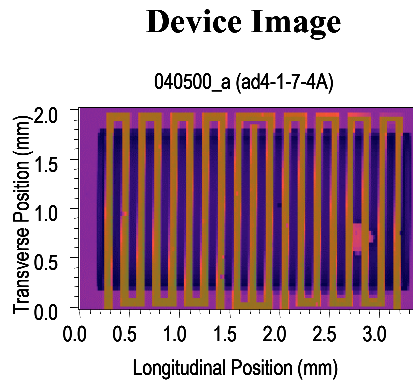

Surface Slope Images

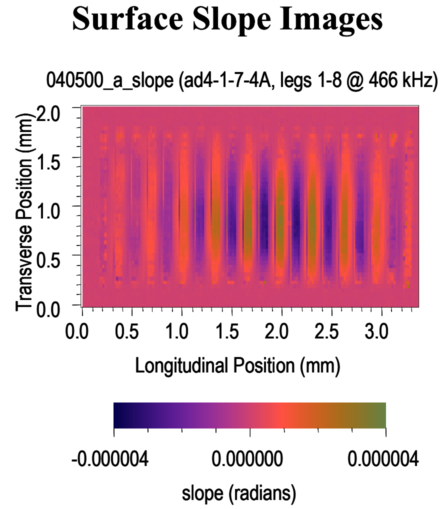

Broadband Spectrum Measured by Driving Only One Transducer

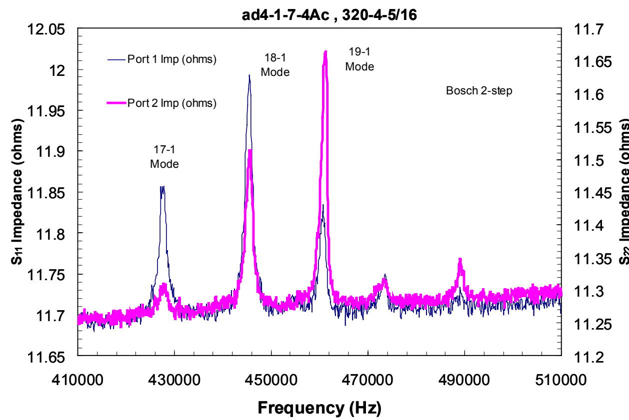

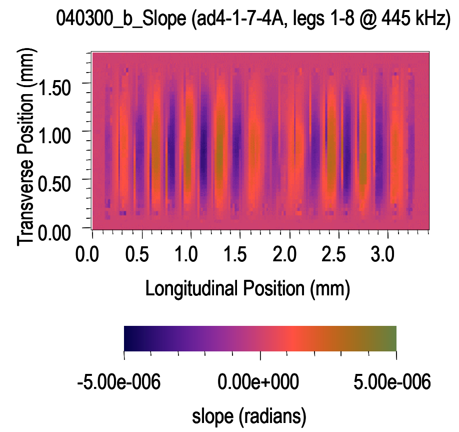

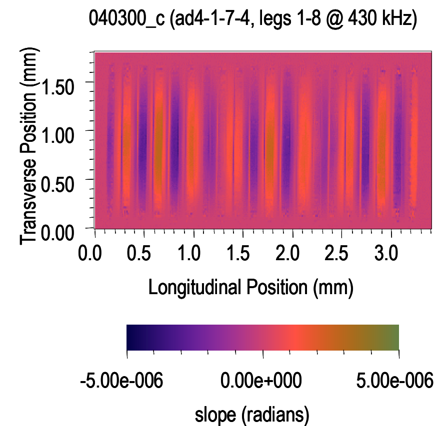

Figure 30. Mode images taken from the second membrane of the same FPW chip used to generate Figure 29. The shape of the impedance response is very similar between the two figures, although the frequency range is lower in this figure for data taken at a later time. The surface slope images clearly show the 19 x 1, 18 x 1, and 17 x 1 modes for the three largest peaks.

Fundamental Mode Resonators

Fundamental-mode resonators are characterized in the basically the same way as the single-port, higher-order resonators discussed above, except that they must be tested in vacuum. This is because the fundamental mode couples efficiently to the ambient and is severely damped at atmospheric pressure. Figure 31 shows the pressure dependence of the impedance response of a typical fundamental-mode resonator.

Because the damping is so low during vacuum operation of these devices they are also easily overdriven, which causes amplitude-dependent stiffening and an accompanying increase in the resonant frequency[6]. This behavior is shown in Fig. 32. Another interesting characteristic of these devices in comparison to the higher-order devices that are typically operated at atmospheric pressure is the much narrower bandwidth. At the lowest power where the response is reasonable symmetric, the bandwidth for this device is less than 10 Hz, in contrast to bandwidths of a few kHz for the higher-order devices.

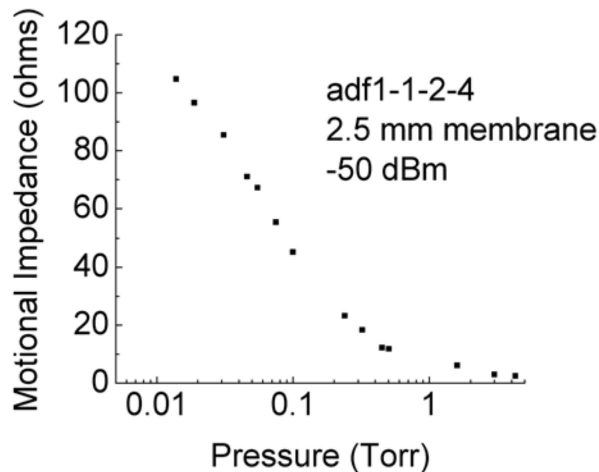

Figure 31. Impedance response of a single-port, fundamental-mode mag-FPW resonator as a function of ambient pressure. Because the fundamental mode couples so well to the ambient these devices must be operated at reduced pressures. This particular device had a 0.25-μm thick amorphous diamond membrane that was 2.5 mm in diameter. The transducer had a DC impedance of about 11 Ω. The ambient pressure must be down to 1 Torr or less to see a significant motional impedance. The resonant frequency of this device was about 54.6 kHz.

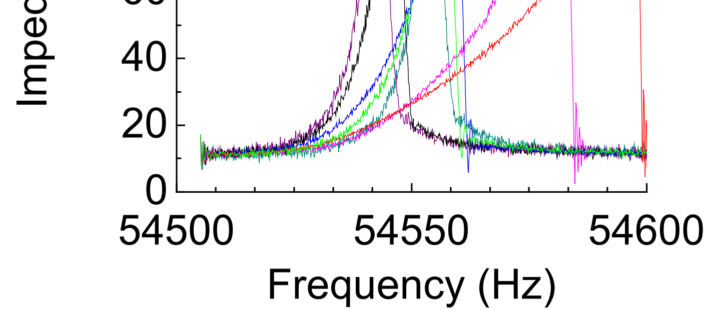

Figure 32. Power dependence of the impedance response of the fundamental-mode resonator from Fig. 31. The asymmetric frequency response arises from amplitude stiffening when the membrane is overdriven.[6] *Note also the very narrow bandwidth of the fundamental mode resonators when operated in vacuum (all of the curves shown in this figure were measured at < 50 mTorr).*

Chemical sensors

One of the most promising applications for the FPW platform is in the area of chemical sensing. We investigated this application using polymer coatings originally developed for surface acoustic wave (SAW) sensors that operate at much higher frequencies (100 - 750 MHz). Standard, two-membrane FPW chips of the type discussed in earlier sections of this report were used for this demonstration.[29]

The devices used in this study include two membranes that are 4.48-mm X 1.60-mm. A picture of a dual membrane chemical sensor chip mounted to a plastic header is shown in Fig. 33. The resonant frequency is nominally 400 kHz. Ethyl cellulose was applied to the back of one membrane with an airbrush to impart chemical sensitivity. As the ethyl cellulose absorbs vapors from the ambient, the mass density of the membrane increases, and the resonant frequency decreases accordingly. The coating used here was approximately 40% the thickness of that used on surface acoustic wave (SAW) chemical sensors at Sandia National Laboratories. The other membrane is left bare to act as a reference for removal of ambient effects other than chemical vapor exposure.

Figure 33. Dual membrane chemical sensor chip mounted to a plastic (PEEK) header.

As mentioned in earlier sections, the resonant frequency of an FPW device operating at atmospheric pressure depends upon properties of both the membrane (such as bending moment, tension, and areal mass density) and the ambient (density, temperature, pressure, viscosity). For chemical sensor applications, we are interested in resonant frequency shifts due to mass loading (changes in the membrane areal mass density). We must eliminate or compensate for frequency shifts due to the other factors. This is most easily accomplished by determining the shift in frequency of a coated device with respect to an uncoated, but otherwise identical reference device simultaneously exposed to the same ambient conditions.

The mag-FPW resonator was characterized with a Hewlett-Packard 8751A network analyzer before and after coating with ethyl cellulose. The FPW device is

loaded into a special test case for initial characterization and chemical testing. The permanent magnets used in this test case produce about 6.5 kG at the membrane. The input power was 1 mW or less. The coating used to generate the data presented in this paper caused a few kilohertz shift in the resonance frequency and slight attenuation (< 2 dB) of the acoustic signal. The two-port oscillator circuit described above was used to drive the mag-FPW chemical sensor during chemical testing. As mentioned earlier, this circuit tracks the resonant frequency by incorporating the output port of the two-port resonator in a feedback loop.

Chemical sensitivity of the coated mag-FPW resonator was determined by challenging the sensor with known concentrations of various chemicals (chloroform, tetrachloroethylene, trichloroethylene, toluene, and xylene). A description of the gas testing system is given in Ref. [30]. Testing was carried out over a wide range of analyte

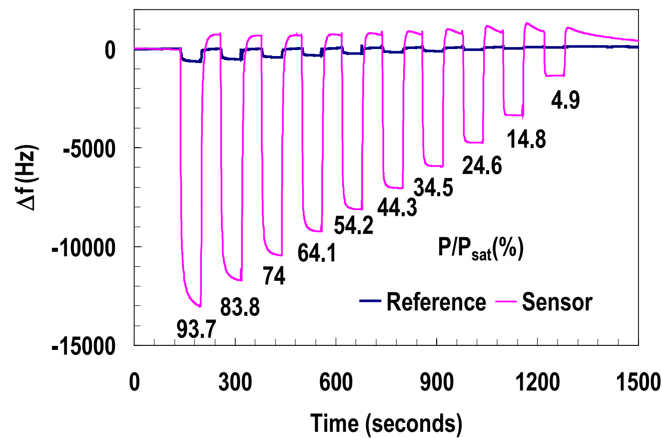

(a)

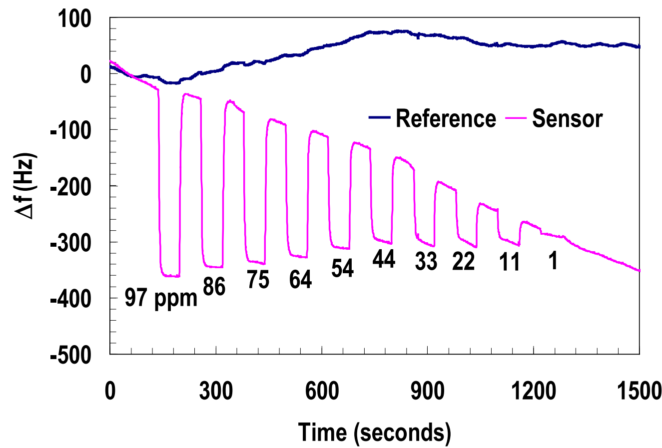

(b)

Fig. 34. This figure shows the real time response of both the reference and coated membranes to high concentration (a) and low concentration (b) chloroform challenges. The percentages are P/P_{sat} for saturated chloroform vapor (15^oC). Notice in panel (a) that although much smaller than the coated membrane response, the reference membrane does show a frequency shift during the chloroform challenges. In panel (b) the reference membrane frequency shows no significant response to the low concentration challenges.

concentration, ranging from P/ P values of 90% to as low as 1 part per million by

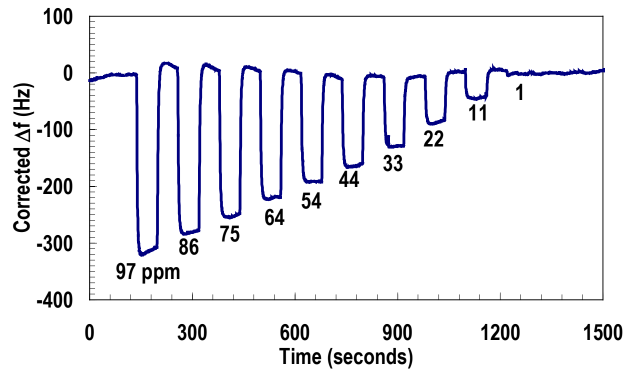

Figure 36. Response of ethyl cellulose coated mag-FPW resonator to low concentration chloroform exposures. Background drift from ambient pressure and temperature effects were subtracted by referring to the simultaneous response of an uncoated twin device and also subtracting the smooth background drift.

In Figs. 35 and 36 baseline and ambient drifts have been removed by subtracting the reference device frequency shift from the coated membrane frequency shift, plus removing any smooth background drift in the coated membrane response. This procedure cleans up the signal considerably, but does not remove the slow recovery effects seen with the high-concentration chloroform exposures. In a system solution, one could lessen this effect greatly by rezeroing before each challenge. This is a common practice in chemical microsensor systems using a preconcentrator to increase the sensitivity. The 1-ppm chloroform challenge is just barely detectable without preconcentration in Fig. 36. Figure 37 shows the response of the same sensor to low concentration xylene challenges. Note that in this case, the 1-ppm challenge is easily discernable.

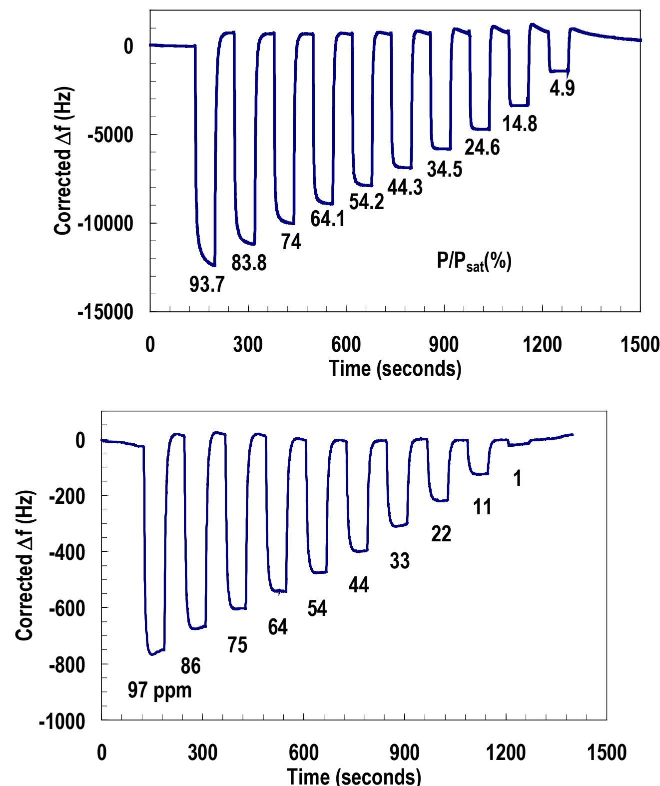

high
slow

Figure 37. This graph shows the response of the same sensor to xylene challenges.

Accelerometers

A conceptual drawing of the originally proposed FPW accelerometer is shown in Fig. 38. A two-port design was developed to go with the drive electronics discussed above. The chip is designed so that the FPW membrane is situated in a flexible cantilevered beam with a large proof mass at one end. When the beam flexes under an inertial load, tension in the membrane changes, and the resonant frequency adjusts appropriately (Eq. 6). The beam was tapered from one end to the other in an attempt to more evenly distribute the change in tension upon acceleration.

thinned beam

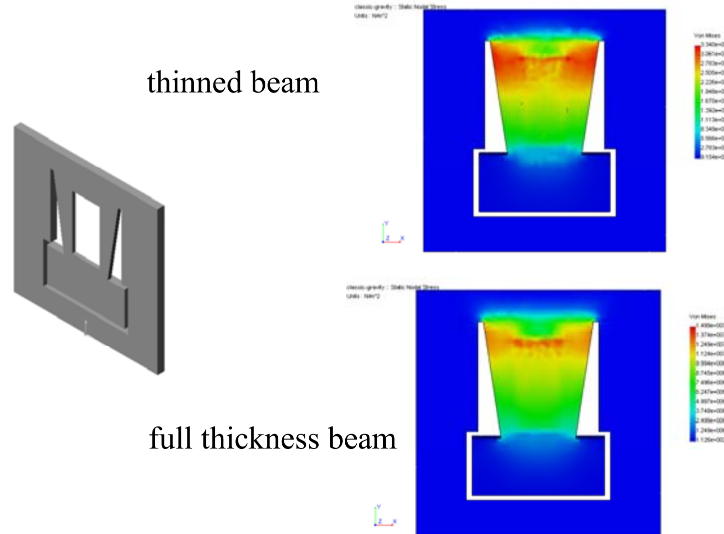

full thickness beam

Figure 39. Finite element analysis showing the distribution of stress in the accelerometer membrane due to the proof mass. The high stress region extends further into the membrane from the hinge point when the beam is thinned.

Finite element analysis (FEA) was performed to determine how well the structure would function. Figure 39 shows FEA results for the basic tapered-beam design, with and without thinning of the beam. In the model, it was not possible to use a true 1-μm thick membrane because of a feature size limitation of the COSMOS/Works finite element package. Qualitative results using a 10-μm thick membrane, however, are expected to give a relative measure of a design's performance. Modeling shows stress in the membrane could almost double if the beam was thinned to 100-microns thick from the original 400-micron wafer thickness.

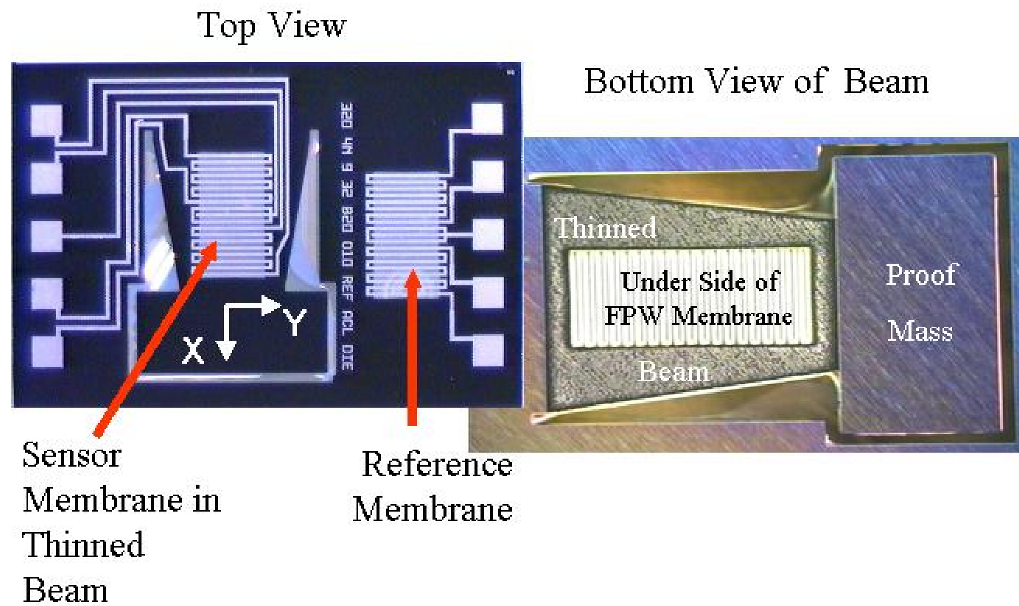

Figure 40. Micrographs of an FPW accelerometer chip with a reference membrane. The sensing membrane is located in a thinned cantilever beam with a large, full thickness proof mass at the end. A close up of the bottom of the beam is shown at the right. The reference membrane is used to compensate for changes in ambient conditions like temperature and pressure, which can also affect the FPW resonant frequency. The X and Y-axes indicated in the picture refer to the tumble axes for the data shown in Fig. 41 below.

These design features were incorporated into the FPW accelerometer chip is shown in Fig. 40. This type of FPW device is feasible only when using the DRIE fabrication protocol because of the complex geometric structures involved (convex angles and multiple thickness elements combined with membrane structures). The chip shown in Fig. 40 also includes a reference membrane for eliminating ambient effects other than acceleration that would affect the resonant frequency. However, all of the data reported here were measured on chips that did not include the reference membrane.

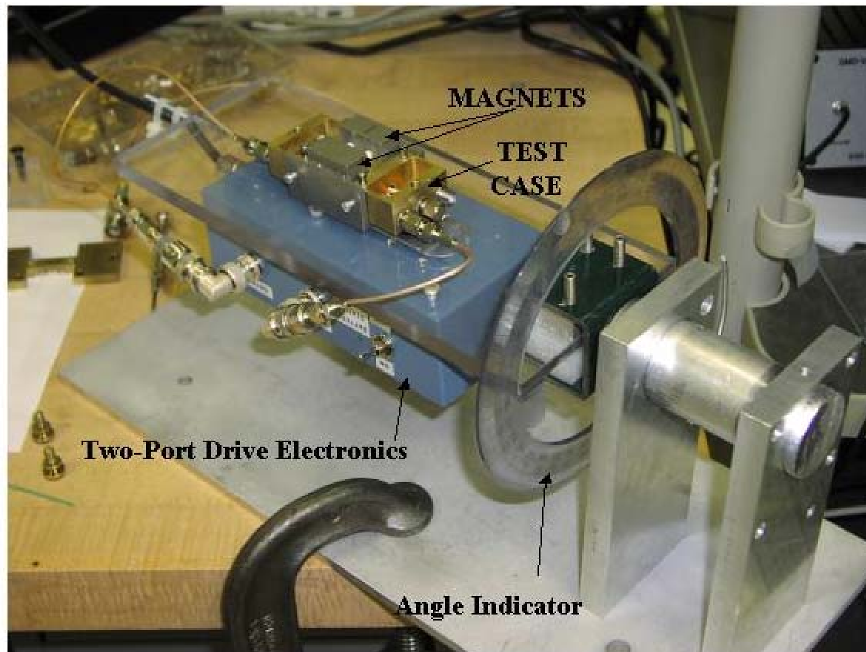

Fig. 41. Picture of the FPW accelerometer tumble tester using the 2-port drive electronics (contained in the blue box). The accelerometer chip can be rotated about different axes by changing how the test case is mounted to the clear Plexiglas platform.

The basic response of the FPW accelerometer was determined using a simple 360 degree tumble test about the sensing axis. The set up used to do this preliminary testing is depicted in Fig. 41. The FPW resonator frequency is tracked using the two-port drive electronics described above. The output of the drive electronics is monitored with a Hewlett-Packard frequency counter and read out over the IEEE-488 bus using a personal computer. The tumble test was taken by rotating the FPW through 360 degrees in preset increments (every 10 – 20 degrees). The mounting platform allows one to rotate the FPW device (loaded in a test case for the measurements show in Fig. 42) about a particular axis, depending upon how the test case is positioned on the stage.

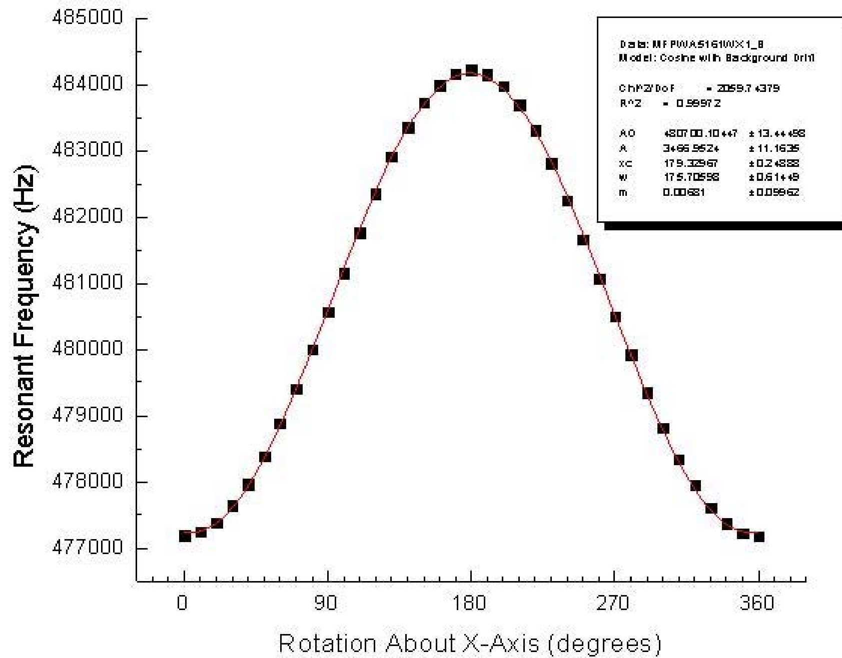

Figure 42. Tumble test data for one of the most sensitive FPW accelerometers built during this project. The red line is a cosine fit to the data. The fit indicates a sensitivity for this particular accelerometer chip of better than 0.5 milli-g's.

The results for one of the better accelerometer chips are shown in Fig. 42. The tumble axes are indicated with respect to the chip as shown in Fig. 40. Rotation about the x or y axes of this particular device reveals sensitivity better than 0.5 milli-g's (assuming 1-Hz resolution in reading the frequency and a shift of 3467 Hz/g as revealed by the cosine fit to the data).

Very few of the accelerometers performed as well as that shown in Fig. 42, because typically these very thin beams were damaged during die separation and handling. Figure 43 shows the results from several accelerometer die taken from the same 100-mm wafer. Note there is a wide range of beam thicknesses. While this allowed us to investigate the dependence upon the beam thickness, the variation was due to the undesired nonuniformity of the DRIE process used to release the beams and membranes. The most sensitive devices from this wafer had only about 1-milli-g sensitivity.

We experimented with increasing the sensitivity of the device by attaching extra weight to the proof mass. This indeed increased the sensitivity, but also caused considerable phase shift of the cosine dependence shown in Figure 42 and even added considerable sensitivity to spinning the die about its z-axis (when the z-axis was horizontal). This distortion occurred because the added mass lies outside the plane of the

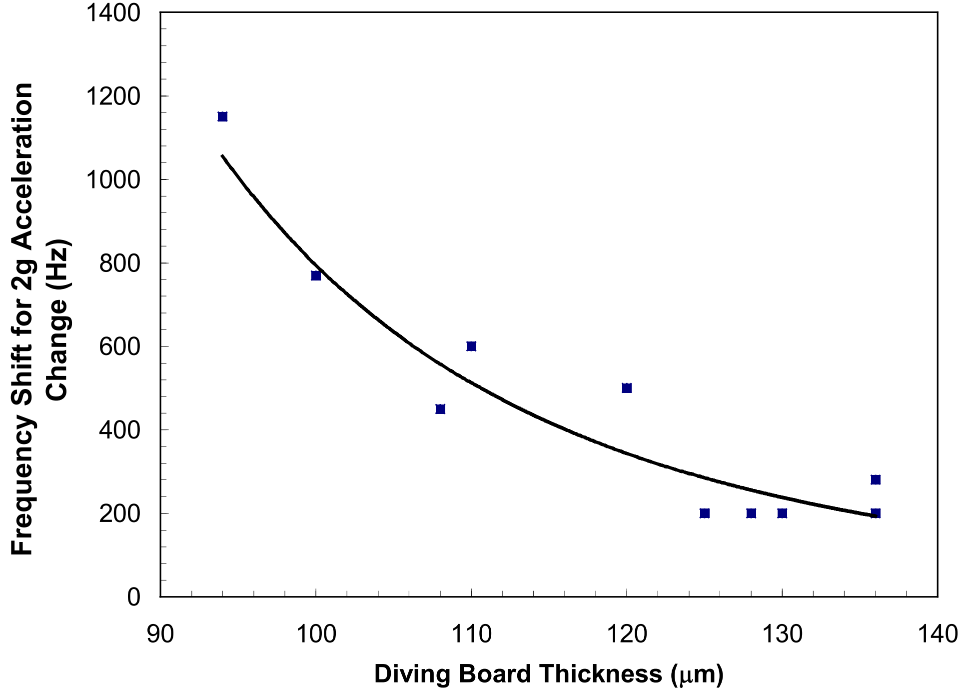

Figure 43. This graph shows the dependence of the accelerometer frequency shift for upon turning the device over (i.e. a 2-g acceleration change). All of these devices came from the same silicon wafer, giving an indication of the typical spread of beam thicknesses. None of these devices were as sensitive (or had as thin a beam) as the champion device from Fig. 42. Many of the thinner beam devices broke during die separation and handling.

beam and makes the proof mass distribution with respect to the beam plane very asymmetric.

While the present results verify the proof of principle for mag-FPW accelerometers, the manufacturability is still suspect. Non-uniform DRIE rates across the wafer lead to many of these effects. This could be improved in a production environment. However, even with better uniformity, the beam has to be so thin to achieve better than 1-milli-g sensitivity that the yield suffers greatly.

We also used finite element modeling to investigate more robust designs. Figure 44 shows a series of panels depicting the deflection of beams with different design characteristics. It was also found that the membrane stress could be increased by about 60 percent if the beam-taper is eliminated and small tab is added at the edge of the membrane. The tab is included to focus the stress loading in the membrane. By both thinning the beam and adding the tab, the tensile stress in the membrane would increase by roughly a factor of four over the tested design. This amplification of stress in the membrane should increase the sensitivity of the accelerometer, but this predicted result has not been verified experimentally. The narrow, constant width of the beam in this design does not allow room for the five connections required for two-port device. Thus

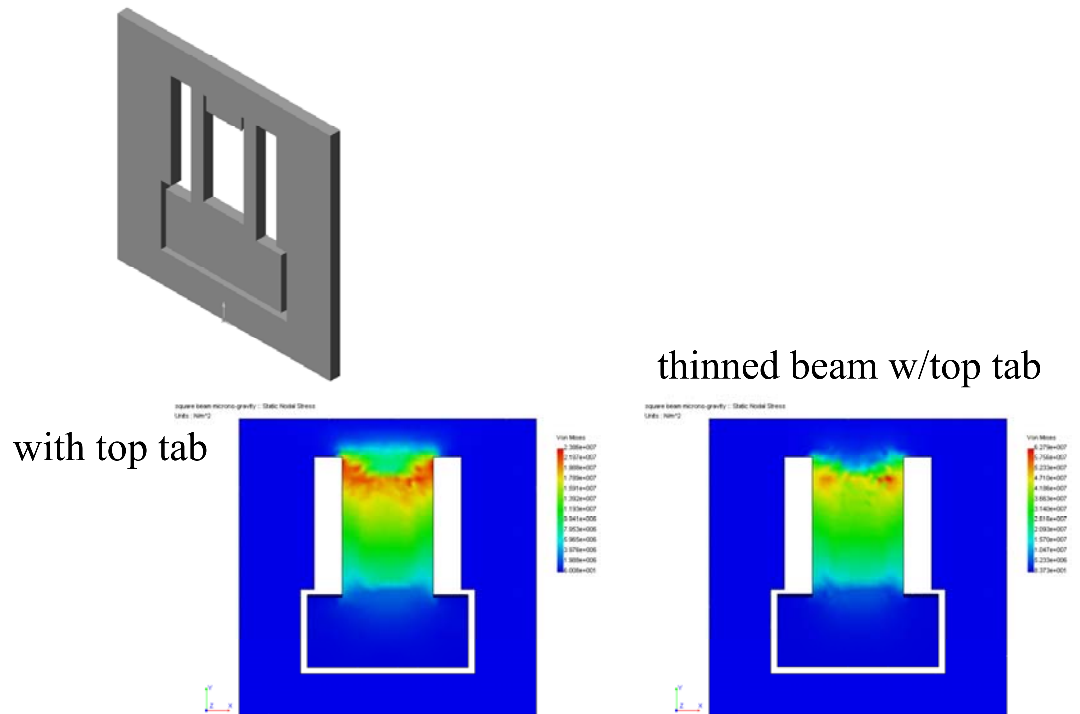

Figure 44. Removing the beam-taper and adding a tab at the top of the membrane could further improve the sensitivity of the accelerometer.

this beam design would have to use a one-port device and the corresponding one-port drive electronics.

Gas Phase Flow Sensors

The temperature sensitivity of the FPW resonator suggests that these structures

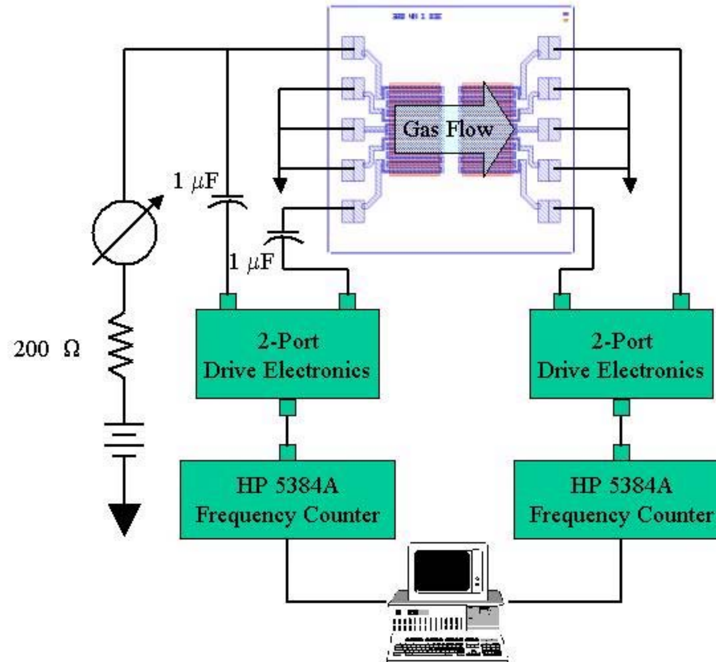

Figure 45. Schematic diagram of the set up used to test an FPW 2-port resonator as a flow sensor. The testing was done with a two-membrane FPW die, but the heater voltage was applied to only one of the membranes. The second membrane was used to measure the indirect heating effects due to conduction through the Si substrate or convection through the flowing gas.

can be configured as flow sensors. By adding a DC current through the input transducer one can raise the temperature of the membrane structure, which lowers the tension and thus the resonant frequency. Any gas flow past the heated membrane should tend to cool it and raise the frequency. Figure 45 shows the set up used to test an FPW 2-port resonator as a flow sensor. The set up uses the portable 2-port drive electronics discussed above (page reference). A power supply and a current limiting resistor (200 Ω) were used to apply the DC heater voltage to the input transducer of the 2-port device. A current meter was used to determine the heater power. Large (1 μF) capacitors are used to block the DC voltage from the drive electronics. A PEEK manifold was attached to the backside of the FPW die to direct the gas flow across the membrane (similar to Fig. 33). These tests were actually done with a dual membrane FPW die, but the heater voltage was applied to only one of the membranes. Any heating of the second membrane came about due to conduction through the Si chip or convection through the flowing gas.

Initial tests were done to determine what magnitude of heater power was needed to facilitate the flow measurement. Figure 46 shows the dependence of the frequency response on the heater power for a wide range of flow rates. One would expect that the

hotter the FPW temperature, the more pronounced the cooling effects due to the flowing gas would be (i.e. larger frequency shifts).

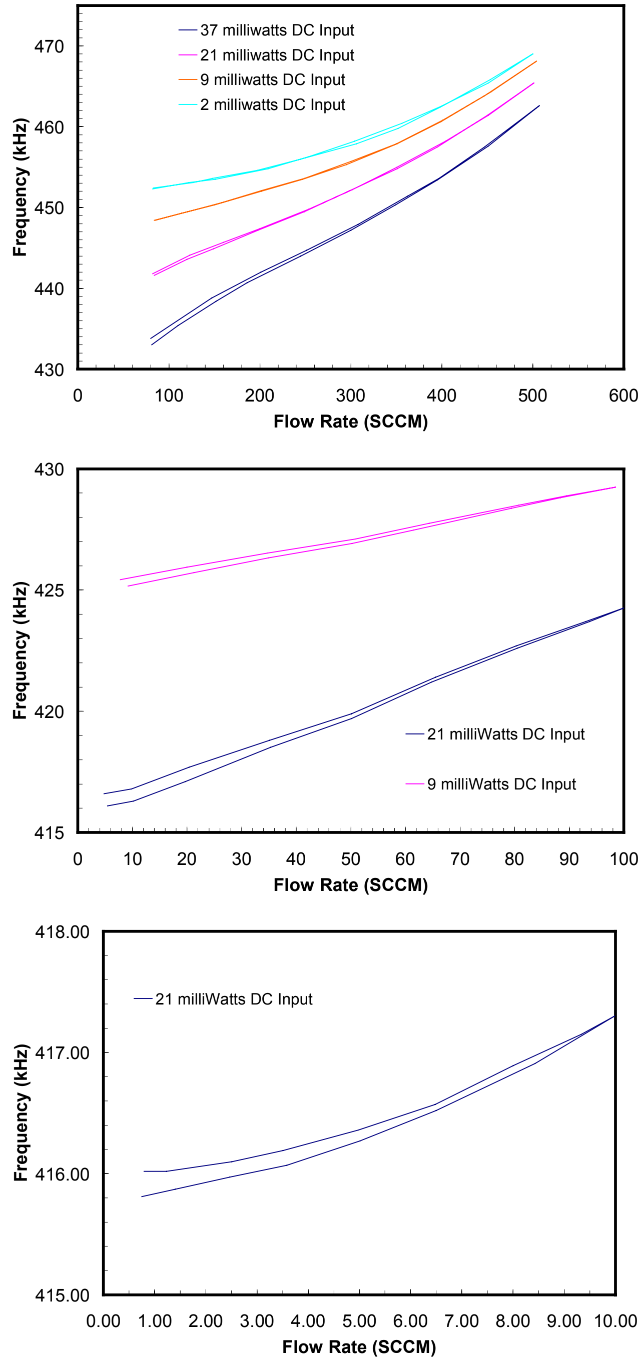

Figure 46. Dependence of the flow sensor frequency shift on the heater power and flow rate.

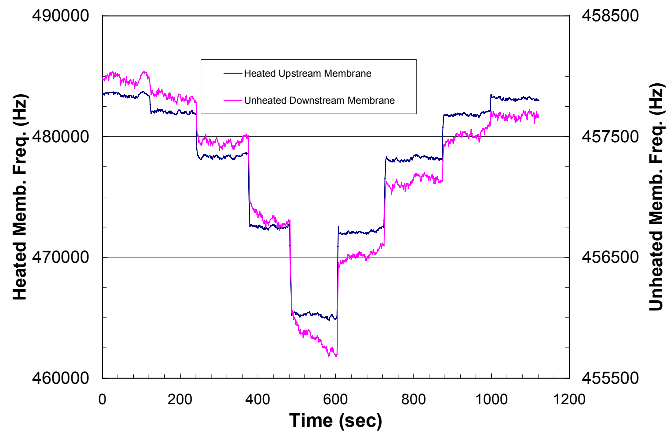

(a)

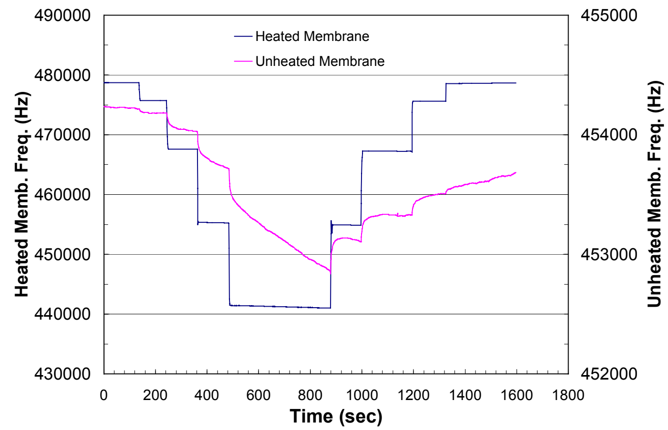

(b)

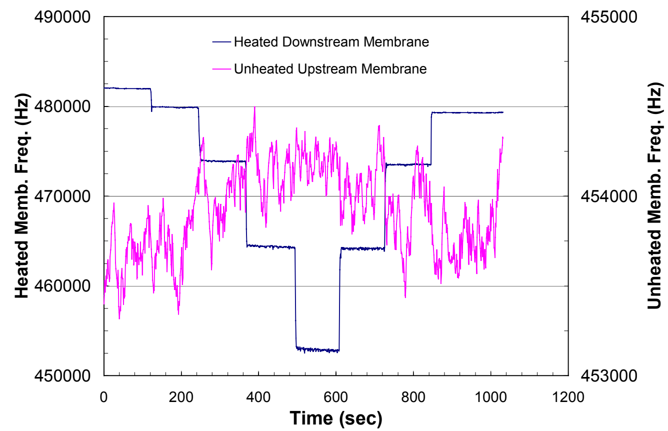

(c)

Figure 47. These graphs compare the response of the unheated with the heated membrane on a dual membrane device. The steps in the response are due to changes in the heater power (2, 9, 21, 37 mW). In (a) the heated membrane is upstream. In (c) the heated membrane is downstream. In (b) there is no flow. Clearly the gas flow dominates the response of the membranes, as expected.

Figure 47 compares the frequency response of the heated and unheated membranes on one of the dual membrane devices. This experiment clearly demonstrates the relative contributions of conduction through the silicon frame and convection through the gas.

The flow testing data taken on the FPW devices demonstrates their suitability as flow sensors. While the addition of the second membrane that is not heated allows one to determine the direction of gas flow, but probably does not add much to the accuracy of the flow measurement.

Liquid Operation

One potential advantage of FPW devices over SAW devices is the ability to operate in liquids. This makes the FPW platform attractive for both sensing and pumping in liquid analyte applications. Liquid operation[31,32] has been demonstrated with piezoelectrically driven FPW devices. However, liquid operation with the present mag-FPW devices was very disappointing. Figure 48 compares the typical response of a mag-FPW resonator in air and water. The severely damped signal in water is no longer suitable for sensing purposes. Similar results were seen with transducer wavelengths ranging from 640 μm down to 100 μm.

Prototype mag-FPW pumping structures were developed as part of this project (Fig. 49.), but were also disappointing in performance. Although momentary motion of microspheres suspended in water was occasionally observed, we were never able to demonstrate consistent movement within the liquid.

Why do the mag-FPW devices not function well in the liquid environment like their piezoelectrically driven cousins? Besides the actuation mechanism itself, the mag-FPW membranes are much thinner than their piezoelectric counterparts. The mag-FPW membrane is made up of a thin (0.5 – 1 μm) low-stress SiN layer, plus the 0.75- μm thick Al metalization. A typical piezoelectric FPW membrane is comprised of a similar SiN layer, a 0.2 μm Pt ground plane, a 2-3 μm thick ZnO layer, and a 0.75 μm Al metalization layer. Thus the piezoelectric FPW membrane is much thicker and stiffer

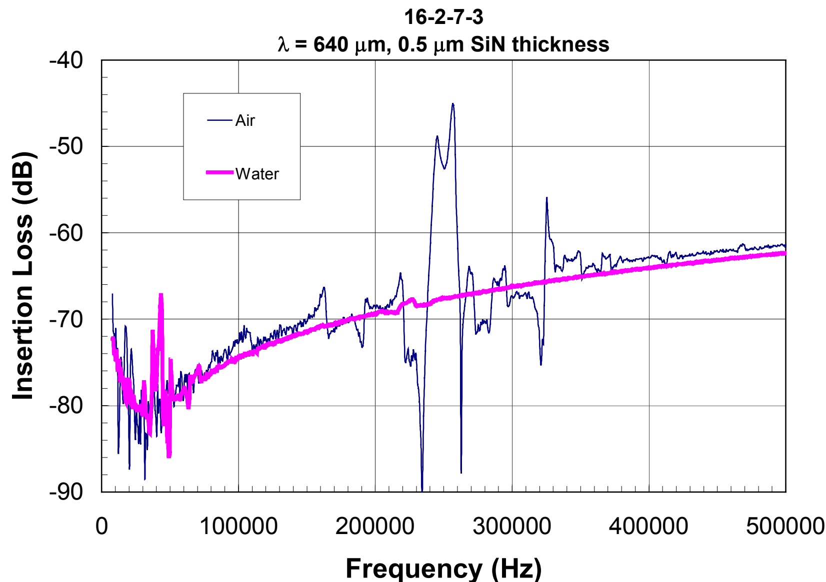

Fig. 48. This graph shows the typical loss of signal with liquid operation with the present mag-FPW devices. The large primary peak in air shifts to lower frequency in water as expected, but is also heavily damped. The severely damped signal is no longer useful for sensing purposes.

than the mag-FPW membrane, and more likely to be dominated by the bending moment, rather than the tension in the film. This may be a more favorable configuration for liquid operation.

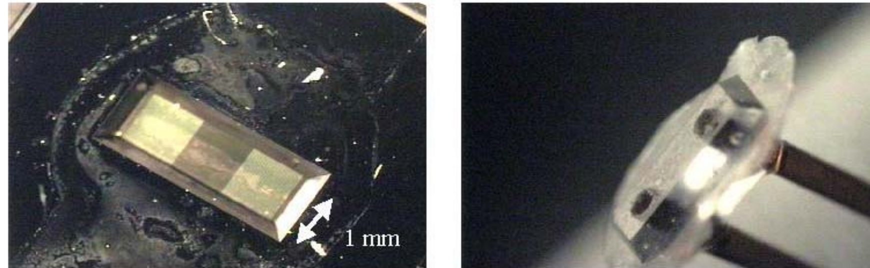

Fig. 49. Optical micrographs of a mag-FPW pump prototype, and the lid fabricated from epoxy to confine the liquid to within 50 μm of the backside of the membrane. The panel at left shows the backside of the membrane of a pumping structure using 100μm wavelength transducers with 25 legs each. The beveled <111> etch planes match the bevel sides of the epoxy lid shown in the right panel that was formed in a Si mold formed using the same photomask as the FPW, but etch only 350 μm deep rather that all the way to the SiN membrane on the front side of the 400-μm thick Si wafer.

Summary and Future Directions

The purpose of this project was to develop the mag-FPW platform for implementation in sensored microsystems. This versatile structure has the potential to fulfill a variety of sensing and actuating functions in such a system. Furthermore, the FPW platform has been shown by others[31,32] to work with either gas or liquid ambient. The lower frequency operation compared to a SAW device simplifies the drive electronics. The mag-FPW platform is simpler to fabricate than the piezoelectric FPW, and so should be easier to integrate with silicon-based control electronics.

How much of this potential has been realized? For a gas environment, we have successfully demonstrated mag-FPW pressure sensors[11], chemical sensors[29], strain gauges[33], accelerometers or vibration sensors, flow sensors, and of course, temperature sensors. The fundamental mode mag-FPW is currently being developed as an acoustic frequency analyzer on a chip as part of another project at Sandia. All of these sensors are based upon the sensitivity of the FPW resonant frequency to the areal mass density and/or tension of the membrane. In spite of the sensitivity of the membrane to a number of external stimuli, we have shown that it is possible to calibrate or compensate for back ground drift using techniques common for such sensor systems (regardless of the transduction method). We have developed field deployable drive electronics in a printed circuit board format for both single and double-port mag-FPW resonators. The double-port drive circuit was also reduced to an ASIC design, but the first chips manufactured at an external foundry were not available during the course of this project.

To date, the mag-FPW platform has not proven itself for use in a liquid environment. The strong signals available with gas operation are almost completely damped out when the membrane is placed in a liquid environment. It is our belief that this poor performance is inherent to the extremely thin, lightweight membrane of the mag-FPW embodiment as compared to the piezoelectrically excited version. This eliminates the mag-FPW from consideration for liquid-based sensing and liquid pumping applications.

We have shown that the mag-FPW resonator can be fabricated using all dry etch techniques that are compatible with post-processing of the device on silicon wafers that have finished control circuitry already present. Low-stress SiN membranes remain the best candidate for this purpose. These membranes can be present during normal CMOS processing without losing their desirable properties. We were unsuccessful in finding other membrane materials that could be deposited at low temperatures in a post processing environment and still be compatible with the dry etch release process. Further work is needed in the development of a polymer-based membrane for the mag-FPW.

Future work on the silicon-based mag-FPW platform should concentrate on the integration of the sensor with the control electronics and other sensor system components (such as a micro gas chromatographic column and a micro preconcentrator). Early attempts at this are underway in the Microelectronics Development Laboratory at Sandia. In addition to the larger, bulk micromachined FPWs used in the present study, smaller dimension (hundreds rather than thousands of microns) mag-FPWs can be made with surface micromachining techniques with either sealed or vented cavities behind the membrane.

In contrast to the silicon-based FPW devices discussed above, we have recently investigated an alternative fabrication protocol based on polyimide flexible printed circuit board technology with the help of Hutchinson Technologies, Inc. (HTI) that promises to be extremely low cost. In an effort to develop a new product line, HTI fabricated several FPW designs in their copper/polyimide flex-circuit board material. This well-established manufacturing technology does not require a clean room production environment, and is considerably cheaper and simpler than the protocol required for the silicon-based FPWs discussed above. The polyimide material acts as the membrane. The copper traces replace the aluminum of the silicon-based FPWs. The silicon frame is replaced by a stainless steel cladding. Minimum dimensions for this technology are only about 3-4 mils (75 – 100 microns), but this is sufficient to replicate many of the silicon-based designs we have investigated so far. One limitation at the present time is that standard flex-circuit layer thicknesses are typically 15-20 μm, rather than the 0.5 – 2-μm thicknesses typical of the silicon-based devices. However, HTI was able to process thinner than normal layers, and produce functional FPWs. Several designs were investigated by finite element modeling, and seven designs were selected for testing. HTI

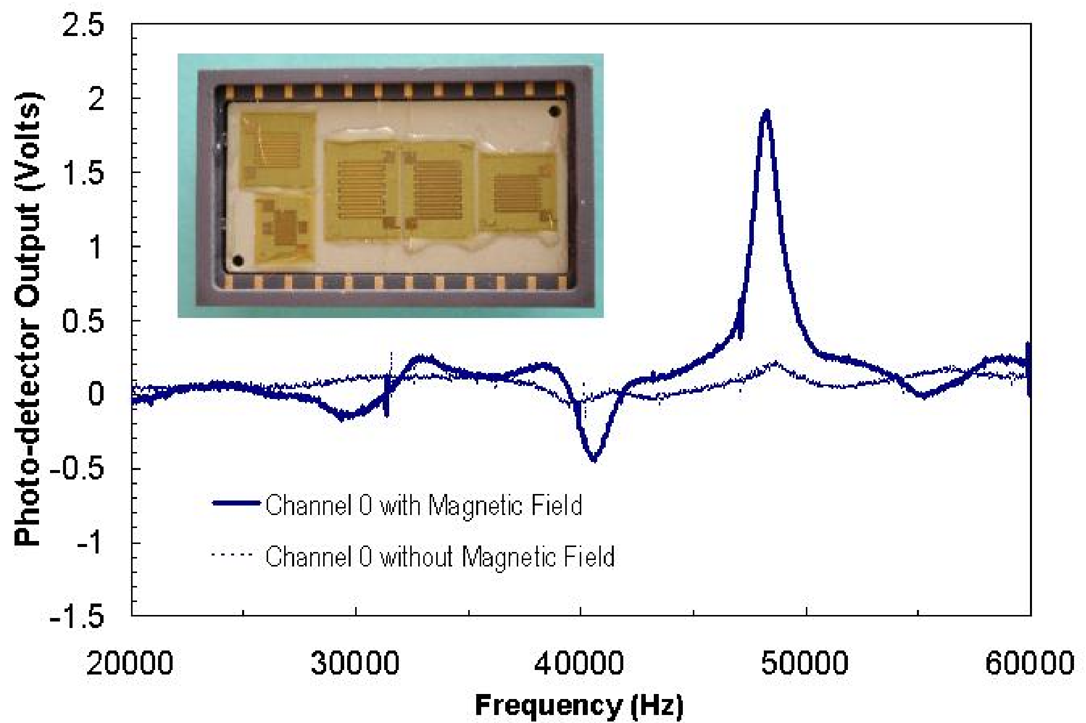

Figure 50. Magnetically excited FPW resonators manufactured by HTI in their flex-circuit board technology. The appearance and disappearance of the major peak just below 50 kHz with and without the magnetic field shows that a flexural plate wave is definitely being excited.

produced a few hundred of these devices on their standard 12" x 27" sheet stock. Five of these FPW designs are shown in Figure 50 after packaging in a ceramic DIP. The individual devices are separated out of the sheet using a scissors. Figure 50 also shows

the measured motion of the membrane surface as a function of frequency for one of the devices. We used our optical imaging set up to determine the frequency of these devices. We were not real sure where to expect the resonant frequencies to occur because we do not know the properties of the polyimide sheet stock very well, and also do not know the amount of preloading that might occur due to packaging. Although the performance obtained in these first efforts are not as good as obtained with the Si-based FPWs, the results show that the polyimide circuit board membranes can be used for FPW devices. The simple and established production methods for these polyimide devices may eventually accelerate commercialization of FPW based sensors.

One final area that must be addressed in a comprehensive fashion regardless of the mag-FPW technology used is the development of small, easily implemented magnetic circuits to supply sufficient magnetic field to drive the resonators. All of our current embodiments use larger dimension magnets (> 6 mm on a side) obtained from commercial vendors. LIGA-like fabrication techniques could be used to produce custom geometries for mag-FPW applications. However, with current materials and fabrication techniques, the B-fields are considerably lower that we obtain with our current magnets.

Appendix A. Bulge Measurements of Membrane Stress

Date: 9/3/98
To: Kent Schubert, Steve Martin and Mike Butler
From: Doug Adkins
Subject: Measuring tension in FPW membranes

By measuring the profile of an FPW membrane that is subjected to a pressure load, it appears that we can get a good estimate of the tension in the membrane. The procedure for making this measurement is described here.

A Swagelock port was glued to the back of a 2-mm fundamental mode device, and a 13.4 kPa (1.9 psi) positive pressure was applied to the port to deform the membrane. The profile of the membrane was measured by Tony Bryce (Dept.1484, phone 845-0932) with a FOCODYN optical probe. The optical probe measures a 1-micron spot radius and it can measure deflections over a range of +/-250 microns at a rate of 10 kHz. Figure 1 shows the measured profile of the membrane with and without the applied pressure.

Membrane tension is determined by doing a simple load balance calculation on the membrane. For the system illustrated in Figure 2, balancing the pressure forces and the tension forces in the y direction implies,

$$\pi\, r^2\ P = -2\pi\, r\, T\, \delta \frac{dy}{dr}\ , \qquad (1)$$

where P is the pressure, T is the tension, and δ is the membrane thickness. This can be integrated to yield,

$$y = \frac{P}{4\, T\, \delta}\left(a^2 - r^2\right)\ . \ (2)$$

where a is the radius of the diaphragm. From the FOCODYN data, it appears the diaphragm was about 1.7 mm in diameter, but I was not sure that the trace was along a centerline through the part. A microscope image shows that the FPW device has a diameter of about 1.67 mm+/-0.1mm (see Figure 3), so it will be assumed that the trace was along a centerline. (If the data was not through a centerline, only a minor modification in the data reduction is necessary to determine the tension.)

A curve fit of the data in Figure 1 shows that the shape of the diaphragm is defined by

$$\begin{aligned} y &= -460.735 + 234.560x - 28.558x^2 \\ &= 28.558\left(\frac{micron}{mm^2}\right)\left[(0.857)^2 - r^2\right] \end{aligned} \qquad (3)$$

where r=x-4.1067mm. (x is in mm and y is in microns). Comparing Eq. 2 and Eq. 3, and setting P=13.4 kPa, we get

$$T\,\delta = \frac{P}{4\left(28.558\,\frac{1}{m}\right)} = 117\,\frac{N}{m}$$

(Of course, we would get the same answer by comparing the curvature of Eq. 3 with $\frac{d^2y}{dr^2}$ from Eq. 1.)

Nobody was sure about the diaphragm thickness of the particular device tested, but Kent thinks that it is a 0.5-micron membrane. Based on the half-micron thickness, the tension in the membrane would be

$$T = 228\ MPa.$$

The bending moments and shear loads were neglected in this analysis. Bending moments would create an inflection near the edges of the diaphragm. Figure 1 shows no sign of an inflection near the edges. If you consider only bending moments oppose deflection in the membrane, then the maximum deflection in the membrane is

$$y_{max} = \frac{3\,P\,a^4\left(1-\nu^2\right)}{16E\,\delta^3}$$

where E is Young's modulus (=$2.7\text{x}10^{11}$Pa) and ν is Poisson's ratio (=0.24) (R.J. Roark, Formulas for Stress and Strain, 1954). For the maximum deflection observed in Figure 1, the imposed pressure would have been only 7.7 Pa. This result implies that bending moments are insignificant in opposing the 13.4 kPa applied pressure.

A similar approach can be used to determine the tension in rectangular membranes. For future measurements, I will build a small vacuum chuck that will both deflect the membrane and hold the FPW in place.

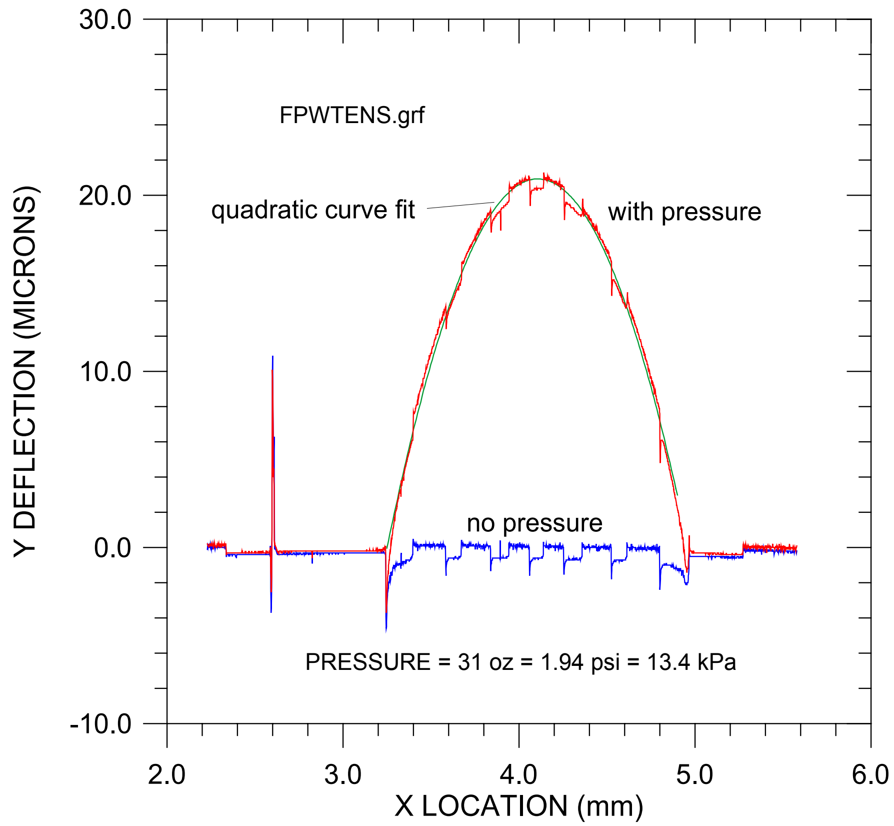

Figure 1. Deflection in a fundamental mode FPW.

.

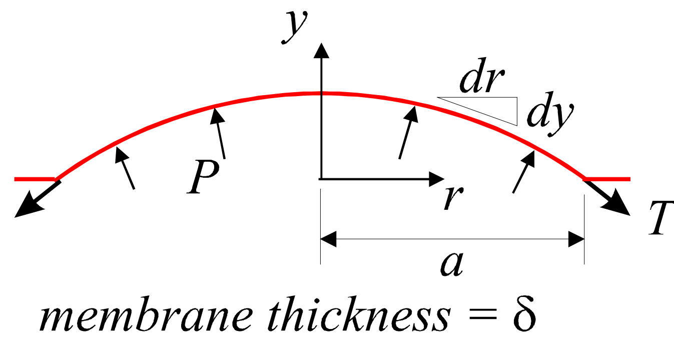

Figure 2. Load balance on membrane.

Figure 3. The tested fundamental mode FPW and a 0.505 mm tube for scale.

Appendix B. Portable Drive Electronics

An FPW's resonant frequency can be measured with a network analyzer, but this equipment is too large and expensive for most applications. In a autonomous sensored system, portable drive electronics are required. During the course of this project we have developed drive electronics for both one and two-port mag-FPW resonators.

Two-Port mag-FPW Resonator Oscillator Circuitry

The FPW oscillator block diagram is shown in Figure B1. One of the main design requirements for a portable sensor-system is that it operates at low power. Frequently power is relatively limited. Another design constraint was that the power dissipated by the FPW must be keep to a minimum. This is due to FPW nonlinearities and power dissipation capability. If the FPW is driven too hard it can be catastrophically damaged due to the large electromagnetic forces on the FPW conductors. This design operates the FPW at approximately 0.2 mW, assuming a 15-Ω impedance. This oscillator comprises four main functions (A1-A4) plus the FPW sensor. Due to multiple design constraints a custom (non-op amp) design was developed.

A1 is a single high-gain non-inverting amplifier and is the most critical part of the design. The relatively high loss (45 dB at 0° phase) of the FPW required a high gain amplifier with low phase-shift. In and of itself this is not a large problem considering that the frequency of operation of the FPW is 500 kHz. To accomplish this at low currents (unity mA for this stage alone) becomes a design problem. A2 is a voltage limiter circuit that provides an amplitude limited square-wave to the buffer amplifier, A3, which drives the FPW. A3 is a unity gain amplifier that is capable of driving the low impedance (15 Ω) FPW sensor. The amplifier A_4 is a 20 dB amplifier that is used to drive the next assembly electronics. The signal level at the output of A_3 is a relatively small (100 mV p-p) square wave that is incapable of driving most counter circuitry, thus A_4 provides a useful signal level for the counter interface electronics of the next assembly.

Simplified schematics for each of the four blocks described above will be shown discussed individually starting with the high-gain stage A_1. Figure B2 is a simplified schematic of the high-gain low phase-shift amplifier used in this design. Q_1 and Q_2 are

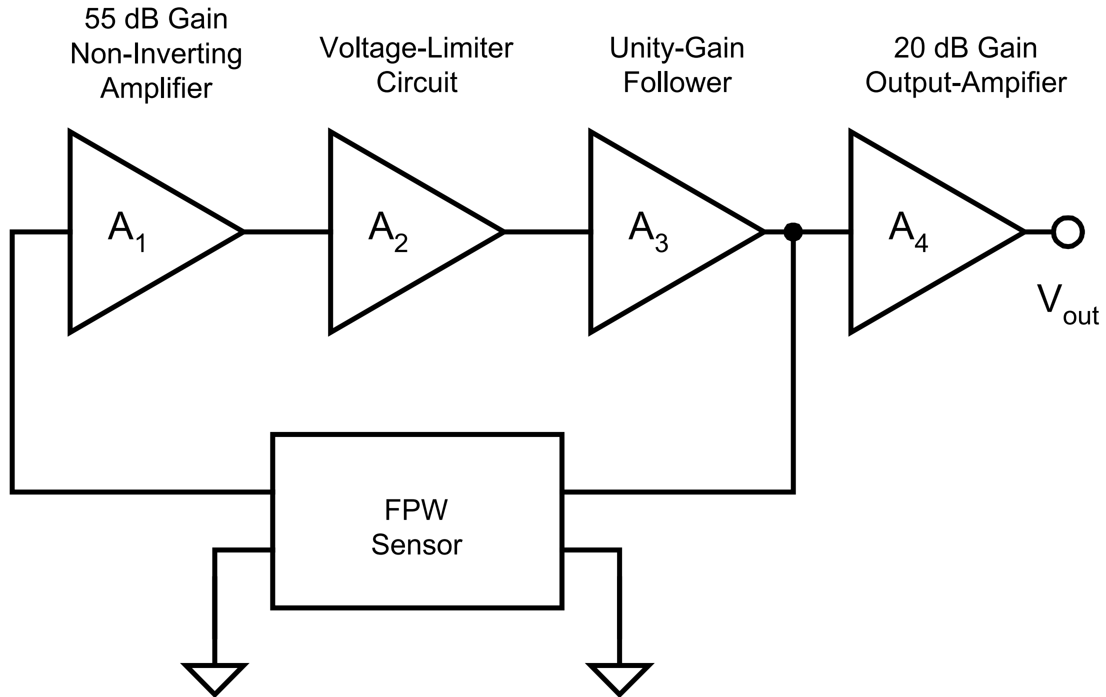

Figure B1. The FPW oscillator block diagram.

the gain elements of the differential amplifier where Q_3 and Q_4 are an active-load which provides a large gain (V_{out}/V_{in}) while minimizing any Miller effect on the input impedance at the base of Q_1. Equation 1 describes the gain, A_v of this amplifier where $A_v=V_{out}/V_{in}$.

$$A_v \cong Z_c /((V_T / I_1) + R_e) \qquad \textbf{(7)}$$

V_T is equal to 26 mV at 25° C and R_e is the bulk emitter resistance (Q_1 and Q_2) equal to approximately 10 ohms.

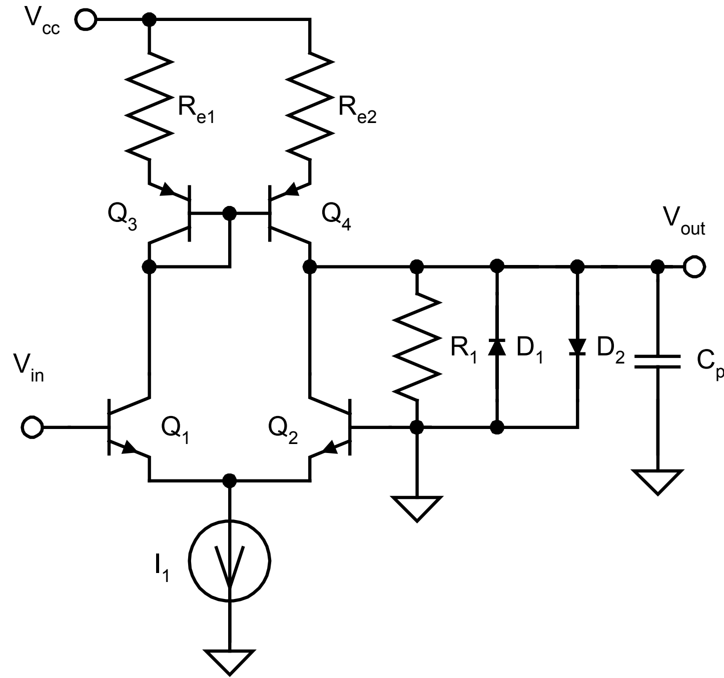

Figure B2. Simplified schematic of circuit block A_1.

For this circuit Z_c is equal to R_1 in parallel with the reactance of C_p in parallel with the output impedance of the differential amplifier. Diodes D_1 and D_2 are used to limit the amplitude of the collector voltage swing (Q_2) to approximately 1.4 V peak to peak. This helps maintain a symmetrical waveform around ground at the collector of Q_2 and prevents overdriving the input to the next stage. Letting R_o equal the output impedance of the amplifier, R_o equals $4(V_A/I_1)$ where V_A is the early voltage of the transistors. For the transistors used in this design V_A is approximately 15 V. I_1 was set to 2.6 mA with R_1 chosen to be 30 kΩ. With these values the voltage gain of the amplifier is approximately 650 or 56 dB. C_p is a combination of transistor and board parasitic capacitance. This capacitance is approximately 5 pF and causes both a gain limiting and phase-shifting of the gain A_v. To provide high-gain (55 dB) and low phase-shift (< 12°) the current I_1 must be set relatively high with R_1 relatively high. R_o in parallel with R_1 must be set to an impedance of approximately five times the reactance of C_p to obtain an amplifier phase shift of < 12°. For the lowest possible operating power C_p must be minimized. To achieve sub-pico Farad capacitances for C_p an analog ASIC would be required. If either the loss of the FPW is decreased or the capacitance C_p is decreased the amplifier can provide a phase-shift closer to the 0° ideal. For the optimal frequency stability it is best to operate the oscillator at the maximum phase-slope (dθ/df) of the FPW. This occurs at the zero phase point of the FPW transmission response characteristics. It is not crucial to make the gain function perfectly real (0° phase-shift) since the transmission response phase-slope is approximately the same from 0° to ±20° degrees of phase-shift. Operating too far away from the zero phase point will decrease oscillator stability and also require higher gain, therefore power, to oscillate.

Figure B3 is a simplified schematic of the voltage limiter block, A_2 from Figure B1. This circuit acts as a follower circuit until the input is driven large enough to force this circuit into limiting. The output will limit to a value of $\pm I_1 R_1$. In this design I_1 is set to 0.13 mA with R_1 equal to 390 Ω. This provides a limiting voltage of ± 50 mV, or 100 mV peak to peak.

This limiting amplifier has an output impedance equal to R_1. Since the FPW input impedance is significantly less than this value the limiter cannot be connected directly to the FPW device and maintain the desired function. A unity-gain buffer circuit, A_3 in Figure B1, provides the necessary buffering. Figure B4 is a simplified schematic of this buffer circuit. Q_1 through Q_4 is a standard differential amplifier configuration. Q_5 through Q_8 comprise a class-B follower circuit that buffers the low-current differential amplifier. The output of the class-B buffer is feedback to the differential amplifier (base of Q_2) which creates a high-performance follower circuit. This design has low offset currents and voltages and provides a very low (< 1Ω) output impedance. This function can be operated at low power due to the high efficiency provided by class-B operation of Q_5-Q_8.

The value of R_1 sets the bias current of the output stage. R_1 is 5 kΩ and sets the idle current of the output transistors to approximately 600 μA. This current (600 μA) is

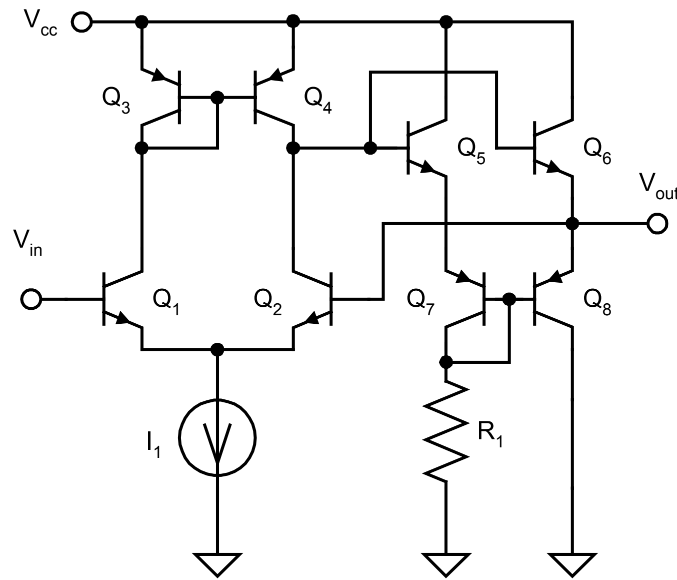

Figure B4. The unity-gain follower circuit.

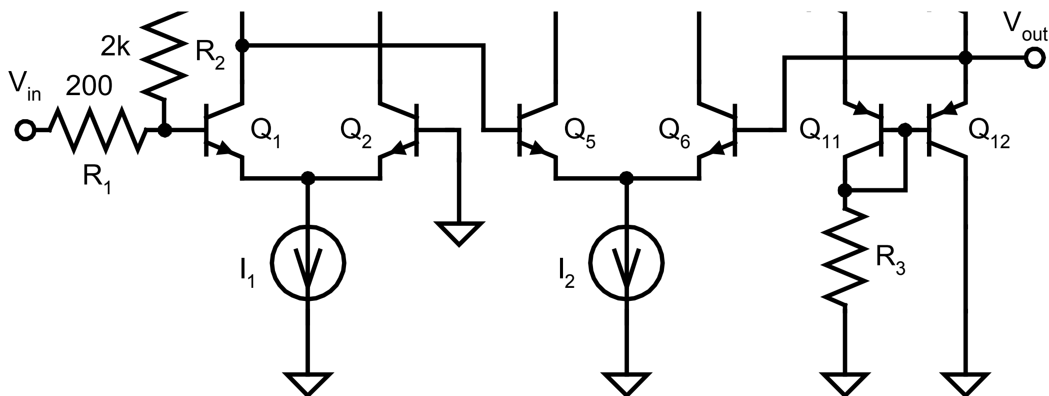

Figure B5. Schematic of the output amplifier of the FPW oscillator.

The differential amplifier Q_1-Q_4 is a feedback controlled inverting amplifier. Feedback resistors R1 and R2 set the amplifier gain. This gain is equal to the ratio R_2 to R_1. For this application the gain was set to 10 (20 dB). Transistors Q_5-Q_{12} is unity-gain buffer amplifier that is the same as the circuit described for Figure 15. The complete amplifier circuit raises the 100 mV peak to peak signal driving the FPW up to approximately one-volt peak to peak. This signal is used to drive the next assembly, which consists of counter circuitry. This circuit uses a total of 2.4 mA.

The total FPW oscillator circuit, A1-A4 plus the bias circuitry, not described here, draws approximately 10 mA. The total power supply voltage is 10 V, (±5) therefore this circuit consumes 100 mW. This current could be brought down significantly if the FPW loss is decreased and/or the parasitic circuit capacitance (C_p) is decreased. It would be possible to make such a design operate at 5 to 6 mA given careful design and control of the circuit parasitics.

1-Port Hand-Held Instrumentation

The single-port drive system is shown schematically in Figure B6. The FPW is placed in series with a current viewing resistor (CVR), and the circuit is driven with a MAX038 high frequency waveform generator manufactured by Maxim. This drive unit uses an RMS detector to determine current through an FPW for a fixed drive voltage. When the FPW resonates, the device impedance increases and a dip occurs in the current. A microprocessor is used to track the impedance shift that occurs at resonance. Figure B7 shows the output from the RMS detector as the drive frequency is swept when measuring a 640-µm wavelength single-port resonator. A major resonant peak is observed at 260 kHz. The microprocessor identifies this drop then scans about the point to continually identify the resonant frequency. A packaged one-port tracking unit is shown in Figure B8.

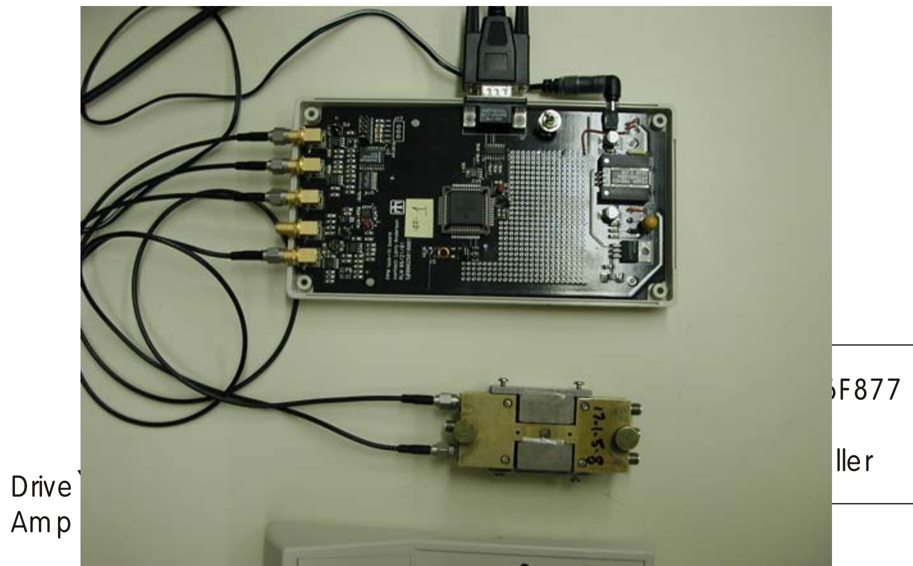

Figure B8. Portable tracking controller for a one-port FPW. Controller circuit is shown at top and an FPW in a brass test case is shown below.

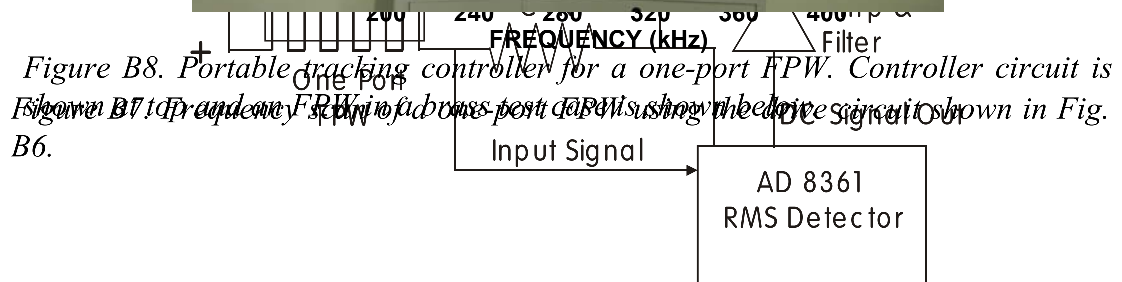

Figure B7. Frequency scan of a one-port FPW using the drive circuit shown in Fig. B6.

Figure B6. Drive electronics for locating peak on a single port FPW.

Appendix C – KOH Fabrication Process for mag-FPWs

Step	Process	Wafers	Description	Comments
1	Start lot	W1-2, C1	W 1-2 use MCNC 0.5 LSN coated, C 1 bare Si witness wafer	
2	HMDS vacuum oven	1-2	backs	
3	PR coat front	1-2	fronts, for protection during the plasma etch	AZ 4330 4 K RPM, 30 s: 110 C, 2 m hotplate softbake
4	PR coat back	1-2	backs	AZ 4330 4 K RPM, 30 s: 90 C, 90 s hotplate soft bake
5	Align	1-2	backs, use **110 Find** from **mfpw99a** mask set (dark field) 5" plate	
6	Develop	1-2	backs	AZ 400 K 1:4, 1 m
7	Nitride etch	1-2	backs	Vacutek or 790 RIE
8	Strip resist	1-2	acetone/methanol strip	
9	Dilute HF dip	1-2	10:1 DI:HF, 30 secs	go to DI rinse for transport to KOH lab
10	KOH etch	1-2	85C, 20 min.	
11	DI rinse	1-2		
12	Measure misorientation	1-2	examine fork array	determine misorientation & record
13	Initial stress measurement	W1, C1	Flexus system	
14	Oxide deposition	W1-2, C1	1 micron thickness	
15	Oxide thickness measurement	C1		
16	Stress measurement	W1, C1	Flexus system	
17	Oxide anneal	W1-2, C1	800 C for 1hour in O2 or air - ramp up and down in O2	want to densify the deposited oxide to improve its insulating properties
18	Oxide thickness measurement	C1		
19	Stress measurement	W1, C1	Flexus system	
20	HMDS vacuum oven	1-2	fronts	
21	PR coat front	1-2	fronts	AZ 4330 4 K RPM, 30 s: 90 C, 90 S softbake
22	Photo align	1-2	***FRONTS***, use ***field_ox*** level from ***mfpw00a*** mask set	align to the 110 find targets, using front-to-back alignment; there is a lot of slop so alignment is not critical; this is to remove the field oxide from the membrane area
23	Photo develop	1-2	fronts	AZ 400 K 1:4, 2 m
24	Oxide wet etch	1-2	fronts, be sure the oxide is completed cleared in the membrane areas	HF etch
25	Strip resist	1-2	acetone/methanol strip	
26	Measure oxide thickness	1-2	Alphastep measurement	
27	HMDS vacuum oven	1-2	backs	AZ 4330 4 K RPM, 30 s: 120 C, 90 S softbake

28	PR coat front	1-2	fronts, for protection during the plasma etch	AZ 4330 4 K RPM, 30 s: 90 C, 90 S soft bake
29	PR coat back	1-2	backs	align to the 110 find targets, compensating for the misorientation calculated in step 12. Alignment is especially critical with the shorter wavelengths.
30	Photo align	1-2	backs, use **KOH_BACK** from **mfpw00a** mask set	
31	Photo develop	1-2	backs	AZ 400 K 1:4, 2 m
32	Nitride etch	1-2	backs, be certain windows are fully cleared of nitride	Vacutek or 790 RIE
33	Strip resist	1-2	acetone/methanol strip	
34	Descum/plasma clean	1-2	LFE, 5 W 5 m	
35	Metallization	1-2	fronts,7500 A Al	sputter the metal for better step coverage
36	HMDS	1-2	vacuum oven	
37	Spin on resist	1-2	AZ 5214 E, 5 K RPM, 30 s, 110 C 90 s hotplate softbake	
38	Photo align	1-2	fronts, use new **METAL level** plate from **mfpw00a** mask set (clear field)	expose on MA 6 for 2.1 s vacuum contact *alignment is critical because of the shorter wavelengths*
39	Photo develop	1-2	1:1.4 312 developer	
40	Metal etch	1-2		
41	Strip resist	1-2	acetone/methanol strip	
42	Black wax coat	1-2	fronts	Be sure to coat beyond the oxide rim
43	KOH etch	1-2	85 C, 400 um /1.6 um/min = 250 min	Check every hour to minimize pinholes
44	DI rinse	1-2	***dry carefully***	
45	Black wax removal	1-2	trichloroethylene strip	
46	Sovent clean	1-2	acetone/methanol clean	
47	Measure alignment	1-2		

Appendix D – DRIE Process for mag-FPW Accelerometers

Step	Process	Wafers	Description	Comments
1	Label	1-2, C1	Use wafers obtained from Ron Manginell. They have an oxide layer underneath the Delft low-stress nitride	
2	Solvent clean	1-2, C1		
3	Plasma clean	1-2, C1	PlasmaTherm	30 m O2 clean
4	Deposit PECVD oxide	1-2, C1	Backs of W 1-2, front C1, 1 micron thickness, to act as a hard Bosch mask in tandem with the underlying nitride	
5	Oxide thickness measurement	C1	Front	
6	Oxide anneal	1-2, C1	800 C for 1hour in O2 or air, ramp up and down in O2	want to densify the deposited oxide to improve its insulating and etch properties
7	Oxide thickness measurement	C1		
8	Solvent PR strip/clean	1-2		
9	Piranha clean	1-2	Clean for metal deposition	
10	HMDS	1-2	Vacuum oven	
11	PR Coat	1-2	Fronts	Use the negative resist that allows liftoff with a clear field mask
12	Softbake	1-2	Fronts	90 C, 90 s hotplate
13	PR exposure	1-2	Fronts using *metal_00(3)A* from mask set **mfpwa_00A**	Align roughly to the major flat - all other levels will be aligned to this one
14	Photo develop	1-2		
15	Sputter Al	1-2	Fronts, 7500 A thickness	Cooke
16	Liftoff process	1-2		
17	Solvent PR strip/clean	1-2		

18	UV/ozone clean	1-2		
19	HMDS	1-2	Vacuum oven	
20	PR Coat	1-2	Fronts, to protect the front during the subsequent backside etching	AZ4330, 3 KRPM, 30 s
21	Softbake	1-2	Fronts	120 C, 5m hotplate
22	PR Coat	1-2	Backs	AZ4330, 4 KRPM, 30 s
23	Softbake	1-2	Backs	90 C, 90 s hotplate
24	PR exposure	1-2	Backs, use *Bosch_Hard_00A* plate from **mfpwa_00A** mask set (dark field)	Critical alignment to the metal pattern on the front side of the wafer
25	PR develop	1-2		AZ 400K 1:4 developer
26	Nitride etch	1-2	Open window in nitride layer	Vacutek nitride etch
27	Oxide etch	1-2	Open window in the oxide hard mask - this is under the nitride on these wafers	Vacutek oxide etch
28	Solvent PR strip/clean	1-2		
29	UV/ozone clean	1-2		
30	HMDS	1-2	Vacuum oven	
31	PR coat	1-2	Fronts for etch protection during Bosch etch	AZ4330, 3 KRPM, 30 s
32	Softbake	1-2	Fronts	120 C, 5m hotplate
33	PR coat	1-2	Backs	AZ4330, 4 KRPM, 30 s
34	Softbake	1-2	Backs	90 C, 90 s hotplate
35	PR exposure	1-2	Backs, use *bosch _hard_thinned_00A* from **mfpwa_00A**	align to the metal pattern as accurately as possible.
36	PR develop	1-2		AZ 400K 1:4 developer
37	Nitride etch	1-2	Open window in nitride layer	Vacutek nitride etch
38	Oxide etch	1-2	Open window in the oxide hard mask - this is under the nitride on these wafers	Vacutek oxide etch
39	Solvent PR strip/clean	1-2		
40	HMDS	1-2	Vacuum oven	

41	PR Coat	1-2	Fronts, to protect the front during the subsequent backside etching	AZ4330, 3 KRPM, 30 s
42	Softbake	1-2	Fronts	120 C, 5m hotplate
43	PR coat	1-2	Backs	AZ5740, 4 KRPM, 30 s
44	Softbake	1-2	Backs	90 C, 90 s hotplate
45	PR exposure	1-2	Backs, use *Bosch_Hard_00A* plate from **mfpwa_00A** mask set (dark field)	Critical alignment to the metal pattern on the front side of the wafer
46	PR develop	1-2		AZ 400K 1:4 developer
47	Hardbake	1-2		
48	HMDS	1-2	Vacuum oven	
49	PR coat	1-2	Backs	AZ4330, 4 KRPM, 30 s
50	Softbake	1-2	Backs	90 C, 90 s hotplate
51	PR exposure	1-2	Backs, use *Bosch_soft_00A* plate from **mfpwa_00A** mask set (dark field)	Critical alignment to the metal pattern on the front side of the wafer
52	PR develop	1-2		AZ 400K 1:4 developer
53	Bosch headstart etch	1-2	150 microns	
54	Strip Bosch soft mask	1-2		
55	Bosch etch	1-2	200 microns	
56	Bosch hard strip	1-2	Done in Lola	
57	Bosch etch until membrane release	1-2	This should leave membrane in middle of thinned diving board	
58	Strip PR	1-2	use caution with membranes	

References

1. R. M. White and S. W. Wenzel, *Appl. Phys. Lett.*, **52** (1988) 1653-1655.

2. S. W. Wenzel and R. M. White, *IEEE Trans. Electron Devices*, **ED-35** (1988) 735.

3. T. Giesler and J.-U. Meyer, *Sensors and Actuators B*, **18-19** (1994) 103-106.

4. M. A. Butler, S. J. Martin, J. J. Spates, and M. A. Mitchell, *Tech. Dig.*, 1997 Int. Conf. on Solid-State Sensors and Actuators, Chicago, June 16 - 19, 1031-34.

5. S. J. Martin, M. A. Butler, J. J. Spates, W. K. Schubert, and M. A. Mitchell, *Proc. 1997 IEEE Int. Freq. Ctrl. Symp.*, Orlando, FL (1997) pp. 25-31.

6 S. J. Martin, M. A. Butler, J. J. Spates, M. A. Mitchell, and W. K. Schubert, *J. Appl. Phys.* **83**(1998) 4589-4601.

7. L. D. Landau and E. M. Lifshitz, *Theory of Elasticity*, 3rd ed. (Pergamon Press, New York, 1986), Ch. 2 and 3.

8. Z. Škvor, *Vibrating Systems and their Equivalent Circuits* (Elsevier, New York, 1991) Sect. 2.3.2.

9. K. F. Graff, *Wave Motion in Elastic Solids* (Dover, New York, 1975) Ch. 4.

10. S. F. Adam, *Microwave Theory and Applications* (Wiley, New York, 1973), p. 271.

11 M. K. Hill, *A Model of a Fundamental-Mode Lorentz Force Actuated Flexural Plate Wave Resonator* (Massachusetts Institute of Technology, 1999).

12. R. J. Shul, C. J. Willison, and L. Zhang, "Selective deep silicon trench etch with dimensional control," SPIE Proc. 3511, 252 (1998).

13. K. E. Petersen, "Silicon as a Mechanical Material," Proc. IEEE 70, 420-457 (1982).

14. W. Lang, "Silicon Microstructuring Technology", Materials Science and Engineering, R17 1-55 (1996).

15 . C. P. D'Emic, K. K. Chan and J. Blum, J. Vac. Sci. Tecnhnol. B10, 1105 (1992).

16. M. Francou, J. S. Danel and L. Peccoud, Sensors and Actuators A 46-47, 17 (1995).

17. Patent No. 5501893: Method of Anisotropically Etching Silicon. Inventors: Franz Laermer, and Andrea Schilp of Robert Bosch GmbH. Issued March 26, 1996.

18. A. A. Ayon, C. C. Lin, R. A. Braff, M. A. Schmidt, R. Bayt, and H. H. Sawin, Solid-State Sensor and Actuator Workshop, 41 (June, 1998).

19. A. A. Ayon, R. A. Braff, C. C. Lin, H. H. Sawin, and M. A. Schmidt, J. Electrochem. Soc. 146 339 (1999).

20. C. Seung-Bok Lee, S. Han, N. C. MacDonald, Solid-State Sensor and Actuator Workshop, 45 (June, 1998).

21. P. A. Clerc, L. Dellmann, F. Gretillat, M. A. Gretillat, P. F. Indermuhle, S. Jeanneret, Ph. Luginbuhl, C. Marxer, T. L. Pfeffer, G. A. Racine, S. Roth, U. Staufer, C. Stebler, P. Thiegaud, and N. F. de Rooij, J. Micromech. Microeng. 8, 272 (1998).

22. R. J. Shul, C. G. Willison, and L. Zhang, SPIE 3511, 252 (1998).

23. R. J. Shul, C. G. Willison, C. T. Sullivan, S. H. Kravitz, and T. E. Zipperian, Electrochemical Society Proceedings, Vol. 98-2, 564 (1998).

24. USC Information Sciences Institute, 1999, MEMS Clearinghouse WEB Database, http://mems.isi.edu/mems/materials/properties.cgi.

25. Hammond, P., 1975, Electromagnetism for Engineers, Pergamon Press, NY, pp. 106.

26. SRAC, 1997, COSMOS/M Advanced Modules Manual, Structural Research & Analysis Corp, Los Angeles, CA, Chapter 2, Theoretical Background.

27. Tse, F. S., Morse, I. E., and Hinkle, R. T., 1978, Mechanical Vibrations Theory and Applications, 2nd ed., Allyn and Bacon, Inc., Boston, MA, chapter 6.

28. Popov, E. P., 1976, Mechanics of Materials, 2nd, ed., Prentice-Hall, Inc. Englewood Cliffs, NJ, pp. 570.

29. W. K. Schubert, D. R. Adkins, M. A. Butlet, S. J. Martin, M. A. Mitchell, R. Kottenstette, and K. O. Wessendorf, "Chemical Sensing with a Magnetically-Excited Flexural Plate Wave Resonator", Chemical Sensors IV, Electrochemical Society Proceedings Volume 99-23, 332-335 (1999).

30. G. C. Frye and S. J. Martin, Appl. Spectroscopy Rev. 26, 73 (1991).

31. R. M. Moroney, R. M. White, and R. T. Howe, Appl. Phys. Lett. 59 774-776 (1991).

32. Ph. Luginbuhl, S. D. Collins, G. –A. Racine, M. –A. Gretillat, N. F. de Rooij, K. G. Brooks, and N. Setter, Proc. IEEE MEMS97, Nagoya, Japan, 327-332 (1997).

33. R. J. Franco, C. O. Landron, J. C. Moser III, D. R. Adkins, and W. K. Schubert, "Nuclear Explosives Package (NEP) Magnetically-Coupled Instrumentation Development", SAND99-0680, 15-32 (1999).

Distribution List

5	MS-0603	W. Kent Schubert	Dept. 1763
1	MS-0603	Randy J. Shul	Dept. 1763
1	MS-0603	Christi Willison	Dept. 1763
1	MS-0603	Ron Manginell	Dept. 1764
1	MS-0782	Mary-Anne Mitchell	Dept. 5848
5	MS-0892	Doug Adkins	Dept. 1764
1	MS-0892	Larry Anderson	Dept. 1764
1	MS-0892	Stephen J. Martin	Dept. 1707
1	MS-0892	Susan M. Brozik	Dept. 1744
1	MS-1073	Catherine Morgan	Dept. 1738
1	MS-1415	Tom Friedmann	Dept. 1112
1	MS-1425	Darin Graf	Dept. 1763
1	MS-1425	Stephen A. Casalnuovo	Dept. 1744
1	MS-9018	Central Technical Files	Dept. 8945-1
2	MS-0899	Technical Library	Dept. 9616
1	MS-0612	Review & Approval Desk For DOE/OSTI	Dept. 9612
1	MS-0188	LDRD Office	Dept. 1030